UCLouvain

epl

École polytechnique de Louvain

Numerical study of the effect of individual pitch control and yaw dynamics on wind turbines wakes and loads

Author: **Jean-Baptiste CRISMER**
Supervisor: **Philippe CHATELAIN**
Readers: **Matthieu DUPONCHEEL**, **Hervé JEANMART**, **Grégoire WINCKELMANS**
Academic year 2020–2021
Master [120] in Electro-mechanical Engineering

Abstract

With the growing number of wind turbines, the interest on how to optimize the power production at the wind farm level is rising. Several techniques have already been identified to be effective, such as wake redirection or wake mitigation. One drawback of such strategies is the increased loads it induces. Control strategies such as Individual Pitch Control (IPC) have shown great potential at reducing the loads. In this Master's Thesis we investigate power optimization strategies based on yaw, along with the effect of combining them with load reducing IPC. The investigations are carried out through numerical simulations with an accurate LES Vortex Particle-Mesh code. The study focuses on the loads, the power output, the wake, and the potential power gain downstream. First, static yaw misalignment to redirect the wake is addressed. Second, a passive dynamic yaw strategy is considered, named free yaw, intended to lead to enhanced wake dissipation. We have observed that IPC has a quite positive impact on static yaw misalignment, while it tends to significantly reduce the wake dissipation effect for the free yaw. Among the different strategies studied, the best one is finally identified for two inline wind turbines.

Acknowledgements

I would like to thank Professor Philippe Chatelain, the promotor of this Master's thesis, for his time, advice and guidance during this year. I also particularly thank Marion Coquelet for her coaching and her helpful advice : she closely followed the evolution of my work and spent a lot of time in videoconferences to answer all my questions. Thanks also to all the staff of the TFL department, especially Doctor Matthieu Duponcheel who took time to solve a software issue. I also thank the other members of my jury, Professor Hervé Jeanmart and Professor Gregoire Winckelmans for their interest and care.

I would also thank all my relatives who have contributed directly or indirectly to this work. My first thoughts go to my girlfriend Pauline. Her presence and listening during this long journey were really precious. I also thank my family especially my father Paul-Georges Crismer who help me to review this manuscript and participates to check the spelling. Gratitude to Valentin Moëns and Nayan Levaux for their careful review of this document. I thank all the Bioethikot: Clarisse, Florence, Pierre and Gregoire; for listening to all the problems I encountered.

Computational resources have been provided by the supercomputing facilities of the Université catholique de Louvain (CISM/UCL) and the Consortium des Équipements de Calcul Intensif en Fédération Wallonie Bruxelles (CÉCI) funded by the Fonds de la Recherche Scientifique de Belgique (F.R.S.-FNRS) under convention 2.5020.11 and by the Walloon Region.

Contents

List of Figures

List of Tables

Chapter 1

Introduction

1.1 Context and motivations

Climate emergency has driven political ambitions towards decarbonizing our society. The recent climate objectives put forward the need for alternative energy sources [1]. Wind energy technologies are a cornerstone to meet global climate objectives; they are an essential part of most governmental action plans, with an installed capacity projected to keep growing exponentially [2]. Installing wind turbines in wind farm configurations is economically advantageous, but can also disrupt the operation of individual units located downstream. The power extraction of a wind turbine perturbs the inflow by decreasing its velocity and increasing its turbulence. This perturbed flow, called wake, then propagates downstream before being progressively dissipated. In the context of a wind farm, the wake of an upstream wind turbine encounters a downstream wind turbine before it is dissipated. This downstream turbine has therefore a lower power capture potential and faces increased wear risks. Wind turbines currently in operation are mainly controlled individually to optimize their power output and structural loading, but advanced power optimization at the wind farm level requires a global control strategy. This control needs to take wake interactions into account. The minimization of the wakes impact on downstream turbines has been a hot research topic these recent years.

1.2 Power optimization strategies

In the literature, control strategies already exist to improve the power available in the wake and optimize the power production at the wind farm level. It is done through wake redirection or dissipation. Most of them rely on either axial induction control or wake redirection, or a combination of both [3]. All those strategies intend to maximize the power downstream with different actions. In this work, we focus on wake redirection strategies based on yaw to deviate or dissipate the wake.

In axial induction control, the power production of upwind turbines is reduced by deviating the turbines from their optimal tip-speed ratio or blade pitch angle. It causes the velocity slowdown in the wake to decrease, hence allowing larger power capture by downstream wind turbines. This method is considered beneficial as soon as the power gain of the downstream turbines compensate for the power losses of the upstream units. However, the real benefits of such strategies are questionable. Some studies reported substantial gains while others did not [3, 4]. Another more promising approach is dynamic induction control: the induction is varying in time and allows a better wake mixing and thus a faster recovery. A comprehensive comparison of control strategies is available in [5].

Wake redirection encompasses a much more diverse category of control strategies. The simplest redirection technique consists in redirecting the wake by introducing a misalignment angle between the turbine and the inflow. This can be achieved by introducing either a tilt angle or yaw angle. The second option is preferred most of the time. Such strategies have been proven to be really efficient [6, 7]. In this work, we refer to this kind of control as *static yaw*, as it is achieved by a static yaw misalignment with the inflow. Redirection can also be achieved by adapting the blade pitch angle. Individual pitch control can be used either to redirect the wake in one direction or to induce a movement in the wake and increase its mixing and recovery. This last method uses wake redirection with the goal of dissipating the wake rather than just redirecting it. J. Friederik et al. studied extensively this method in [8]. Controls based on wake redirection can thus both redirect or dissipate the wake. A detailed overview of redirection techniques can be found in [6].

The last type of control we will mention is hard to classify as a redirection or dissipation strategy. Dynamic yaw consists in varying the yaw angle in time. Depending on the frequency and amplitude of variations of the angle, it can be redirection, dissipation, or both. Few studies assess dynamic yaw strategies, and only one investigating wind farm power optimization was identified; the strategies presented in [4] rely on active control based on an optimization algorithm. This algorithm uses a wind farm state model and a state estimator. This control is thus quite complex and with high computational costs, making it not practically implementable.

All those strategies have the advantage of increasing the power available downstream. However, their two main drawbacks are power losses and increased loads for the controlled turbine. Part of the wind turbine fatigue loading can be mitigated using a load reducing individual pitch control, IPC [9]. IPC reduces the loading imbalances by dynamically adjusting the pitch angle of the blades.

1.3 Objectives and outline

The goal of this Master's Thesis is to study strategies that minimize the wake interaction using yaw redirection and its combination with IPC. Those investigations are conducted through numerical simulations. The first strategy studied is static yaw redirection. It is one of the most promising strategies for wind farm power optimization. Although it has already been extensively studied, its combination with IPC has only been studied recently by Wang et al. in [10]. We aim to provide a similar study by quantifying the possible power gains and losses, downstream and upstream respectively, but the loads aspect is further developed. Moreover, wake characteristics are also analysed in this work. The second control strategy studied is a dynamic yaw strategy. Current investigations on the subject are not practically implementable because of their complexity, so a simpler control is considered. This study will focus on a passive dynamic yaw strategy: free yaw. Such a strategy is intended to increase the wake meandering and enhance wake recovery. Even if free yaw was almost only considered for small power wind turbines, it is investigated here as a possible strategy for wind farm power optimization. Free yaw is thus tested for a large 5 MW wind turbine along with its combination with IPC. To the knowledge of the author, no similar studies have been conducted yet. At last, wake characteristics are also analysed.

The next chapter presents the simulation tools used for this work. The base controller and IPC are also presented. Then, Chapter 3 discusses the static yaw. Cases without turbulence are firstly presented to get familiar with the core physics. Then more realistic turbulent cases are analysed. In Chapter 4 the investigation results for free yaw are addressed. Then Chapter 5

compares the best scenarios of both the static and dynamic study with simulations of two inline wind turbines. Finally, a conclusion summarizes the major observations and draws perspectives.

Chapter 2

Numerical tools and wind turbine model

This chapter describes the different numerical tools used for this Master's Thesis. First, the Vortex Particle-Mesh (VPM) code used in this work is presented. It is named *VPM* from the resolution method it uses and will be noted in italic to avoid confusion with the method of the same name. It is used to solve the flow dynamics of the different simulations that are discussed in the following chapters. The second section presents the multibody system solver, ROBOTRAN, that is used to model the wind turbines and their dynamics and controls. Another section addresses the coupling between both the VPM code and the multibody solver. Finally, the last section discusses the wind turbine model and its controllers.

2.1 The Vortex Particle-Mesh code

This section treats the resolution method used to solve the fluid dynamics. Firstly, the flow solver is addressed. A description of the immersed lifting lines, used to model the blades, is then presented. Finally, a brief note on the treatment of turbulence is made.

2.1.1 Flow solver

The flow solver used in this work was developed jointly at ETH Zurich and UCLouvain. The following description of its principles is based on [11, 12, 13] and [14] where the interested reader can also find more information. As it will be explained, VPM methods combine the advantages of both vortex particles and meshed methods. The former is known to be particularly well suited for convection-dominated flows and the latter ensures the convergence by reinitializing regularly the particle positions and allows to easily evaluate the differential operators.

From vortex particle methods, VPM methods imply the discretization of the velocity ($\mathbf{u}$)-vorticity ($\omega = \nabla \times \mathbf{u}$) formulation of the Navier-Stokes equation in their Lagrangian form:

$$\frac{D\boldsymbol{\omega}}{Dt} = (\boldsymbol{\omega} \cdot \nabla)\mathbf{u} + \nu \nabla^2 \boldsymbol{\omega}, \tag{2.1}$$

$$\nabla \cdot \mathbf{u} = 0, \tag{2.2}$$

where $\frac{D}{Dt} = \frac{\partial}{\partial t} + \mathbf{u} \cdot \nabla$ denotes the Lagrangian derivative and ν is the kinematic viscosity, instead of the more common velocity-pressure Eulerian formulation. The vorticity field is thus discretized with particles characterized by a position $\mathbf{x}_p$, a volume V_p and a strength $\alpha_p = \int_{V_p} \omega d\mathbf{x} \approx \boldsymbol{\omega}_d V_p$. Those particles are convected by the flow and their strength is modified to account for vortex stretching and diffusion

$$\frac{d\mathbf{x}_p}{dt} = \mathbf{u}\left(\mathbf{x}_p\right), \tag{2.3}$$

$$\frac{d\boldsymbol{\alpha}_p}{dt} = \int_{V_p} \left((\boldsymbol{\omega}\cdot\nabla)\mathbf{u} + \nu\nabla^2\boldsymbol{\omega}\right) d\mathbf{x} \tag{2.4}$$

$$\simeq \left((\boldsymbol{\omega}\cdot\nabla)\mathbf{u} + \nu\nabla^2\boldsymbol{\omega}\right)_p V_p. \tag{2.5}$$

Here the velocity field is recovered thanks to the Helmotz decomposition $\mathbf{u} = U_\infty + \mathbf{u}_\omega$ through the Poisson equation

$$\nabla^2\mathbf{u}_\omega = -\nabla\times\boldsymbol{\omega} \tag{2.6}$$

solved by a fast Poisson solver in the Fourier space [15].

Using the Lagrangian formalism to discretize the vorticity field with vortex particles gives robustness to the calculation method. It also allows to waive constraints usually present in convection problems in classical Eulerian form like the time stability constraint (CFL). On the other hand, those vortex particle methods are known to be subject to Lagrangian distortion [12]. Some regions would become free of particles while others would contain large groups of them. This will weaken the accuracy of the method. To handle this, as previously mentioned, it is coupled with a mesh. The particles are redistributed on the mesh at regular time intervals by interpolating the vorticity from the particles to the node locations. This process is called the remeshing. This mesh also allows to compute efficiently the different differential operators and solve the Poisson equation at lower costs. This dual discretization is the main feature of Vortex Particles-Mesh methods as it offers to take the advantages of both discretization methods.

When it comes to wind turbines, flows are typically complex turbulent ones at high Reynolds numbers. Large Eddy Simulation (LES) will thus be used to reduce the numerical cost. LES implies a filtering of the Navier-Stokes equation. The smaller scales of turbulence are accounted for via a dissipation model rather than being solved explicitly. The new vorticity equation to solve is then an adapted version of Equation 2.1

$$\frac{D\omega}{Dt} = (\boldsymbol{\omega}\cdot\nabla)\mathbf{u} + \nu\nabla^2\boldsymbol{\omega} + \nabla\cdot\mathbf{T}^M \tag{2.7}$$

where $\mathbf{u}$ and $\boldsymbol{\omega}$ are the resolved velocity and vorticity fields, and $\mathbf{T}^M$ the subgrid-scale (SGS) stress model that represents the filtered smaller scales. The model used for this work is a classical eddy viscosity model called Regularized Variational Multiscale (RVM)

$$\mathbf{T}^M = \nu_{SGS}\left(\nabla\boldsymbol{\omega}^s - \nabla^T\boldsymbol{\omega}^s\right) \tag{2.8}$$

where $\boldsymbol{\omega}^s$ represents the small-scales part of the vorticity field. More details can be found in [16].

Concerning the spatial and temporal discretization, a fourth-order finite difference scheme is used to carry out the differential operators and a third-order low-storage Runge-Kutta scheme is used for the time integration.

The numerical simulations were performed on the Lemaître3 supercomputer, allowing parallel computing.

2.1.2 Immersed lifting lines for blade modelling

The blades are modelled with a vorticity line that will generate vorticity in the flow by shedding a vorticity sheet. From the Prandtl lifting line theory, making the assumption of a slender body experiencing an essentially two-dimensional flow, a wing (and thus a blade) can be modelled with a vorticity line bundle that progressively leaves the wing [17]. This is exactly the idea that lies behind the immersed lifting lines. The strength of the vorticity lines can be quantified by the bound circulation $\mathbf{\Gamma}(r,t)$ around the airfoil. For a steady flow, the lift per unit span $\mathbf{L}$ and the bound circulation are related through the Kutta-Joukowski theorem

$$\mathbf{L} = \rho \mathbf{V}_{rel} \times \mathbf{\Gamma} \tag{2.9}$$

where ρ is the air density and $\mathbf{V}_{rel} = \mathbf{u} - \mathbf{u}_{blade}$.

The blade model is characterised by different sections along its span, each corresponding to a certain type of airfoil. For each of these sections, the coefficient of lift C_L as a function of the angle of attack is stored. Knowing the inflow velocity and its relative angle with the blade, the lift can then be computed. The bound circulation and the shed vortices, due to spatial and temporal variations of the circulation, can then be evaluated with Equation 2.9 and the solenoidal property of the vorticity ω. In the Vortex Particle-Mesh method framework the added vorticity is discretized with particles for the treatment to remain fully Lagrangian and thus allowing large time steps [11].

2.1.3 Turbulent and sheared inflow

The turbulent wind model relies on a turbulent velocity field $\mathbf{u}'$ which has been, in this work, generated through Mann's algorithm [18]. The vorticity field of this periodic turbulent flow is computed and then made compact in the unbounded directions through a smooth clipping. Vortex particles are created to carry this turbulent vorticity into the domain through the inflow plane [11].

Shear in the inflow is accounted for via the power law

$$\mathbf{U}(y) = \mathbf{U}_0 \left(\frac{y}{H_{\text{hub}}} \right)^{\alpha} \tag{2.10}$$

where $\mathbf{U}_0$ is the flow velocity at H_{hub} the hub height and α is the shear coefficient. Computed in term of vorticity, it gives

$$\boldsymbol{\omega}(y) = \alpha \frac{\mathbf{U}_0}{H_{\text{hub}}^{\alpha}} y^{\alpha-1}. \tag{2.11}$$

2.2 Multibody system solver

In the previous section, the modelling of the flow and the aerodynamics of the turbine have been discussed. The focus of this section is the turbine proper dynamics that is modelled with a multibody system (MBS) software: ROBOTRAN. Its coupling with the *VPM* will be covered in the next section. Here, a brief description is first given. It is followed by the characterization of the multibody system. Then the solving process of the MBS dynamics is addressed.

The ROBOTRAN environment is an in-house software at UCLouvain developed by the UCL-MEED research group. It is based on a symbolic approach to generate multibody equations, a powerful tool to drastically simplify mathematical expressions and to confer the equations upon a high portability towards other scientific disciplines like control [19]. ROBOTRAN is thus a useful

tool to model the turbine dynamics and implement its controls. The software works in three steps: it starts from a graphical description of the MBS; the MBS equations are then generated by the symbolic translator; these symbolic equations are finally automatically interfaced with the simulator.

2.2.1 System characterization

The wind turbine is decomposed into a mechanical system of N rigid bodies. This multibody system is represented by a tree-like structure where the different bodies are connected together through joints.

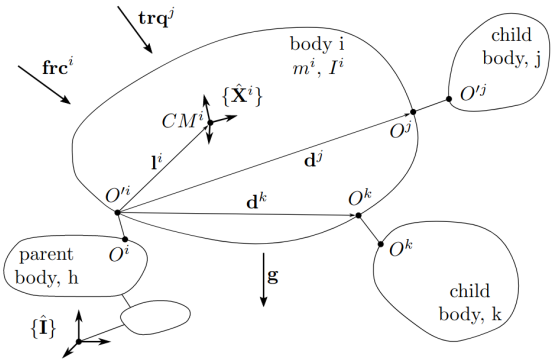

Figure 2.1: Body characterization [19].

A body i is always carried by a parent body h through a joint i and can have children bodies j and k. For any joint i, two reference anchor points are defined: the first one, O^i , on the parent body h and the second one, O'^i , on the body i. Each body is attached with a right-handed frame at its centre of mass and characterized by the vectors that locate the connection points to the other bodies $\mathbf{d}^j$, the position vector of its centre of mass $\mathbf{l}^i$, its mass m^i and its inertia tensor with respect to its centre of mass $\mathbf{I}^i$. This is depicted in Figure 2.1.

The joints specify the displacement to go from the frame of body i to $i+1$. It can either be a translation or a rotation along an axis. In ROBOTRAN, each joint only has one degree of freedom and is thus either *prismatic* or *revolute*. The relative motions that occur in the joints connecting the different bodies are described by relative generalized coordinates $\mathbf{q}$ and their time derivatives $\dot{\mathbf{q}}$ and $\ddot{\mathbf{q}}$. The absolute configuration of the MBS is computed in terms of these relative coordinates and time derivatives.

The forces and torques that act on the bodies are split into the gravitational force $\mathbf{g}$, the joint forces/torques that act via the joint connections Q^i and the external forces. The external forces represent all other forces gathered in a resultant force $\mathbf{frc}^i$ and a resultant torque $\mathbf{trq}^i$ for each body.

2.2.2 Multibody formalism

The system being characterized, the direct dynamics of the MBS is needed to compute the generalized accelerations for a given configuration. The dynamic equations of the whole multibody system are thus generated. The problem can be expressed in a semi-explicit formulation, also called direct dynamics model

$$\mathbb{M}(\mathbf{q},\delta)\ddot{\mathbf{q}} + \mathbf{c}(\mathbf{q},\dot{\mathbf{q}},\delta,\mathbf{frc},\mathbf{trc},\mathbf{g}) = \mathbf{Q}(\mathbf{q},\dot{\mathbf{q}}) \tag{2.12}$$

where $\mathbb{M}$ is the symmetric generalized mass matrix of the system, $\mathbf{c}$ is the non-linear dynamic vector containing gyroscopic, centrifugal, gravity terms and contributions of external forces and torques. $\mathbf{q}$ represents the relative generalized coordinates and $\mathbf{Q}$ is the associated generalized joint forces and torques.
It can also be expressed in a more compact formulation of these equations, where the generalized accelerations are implicitly expressed, and referred to as inverse dynamics model

$$\mathbf{Q}(\mathbf{q}, \dot{\mathbf{q}}) = \phi(\mathbf{q}, \dot{\mathbf{q}}, \ddot{\mathbf{q}}, \delta, \mathbf{frc}, \mathbf{trq}, \mathbf{g}) \tag{2.13}$$

The above models are then obtained by ROBOTRAN through different formalisms [20]. This MBS solver main feature is the generation of the symbolic equations that aims to take advantage of both numerical and manual techniques. It allows the automation of the computational process, on one hand, and arithmetic and trigonometric simplifications, on the other hand. The analytical expressions of the equations are organized and prioritized in a tree structure, which is further optimized to result in a minimum number of operations.

2.3 Coupling of the flow and multibody solver

In the two previous sections, we described the flow solver and the multibody solver. The first one computes the flow dynamics as well as the aerodynamic forces on the blades. While the second one solves the dynamics of high number of degrees of freedom systems. The two systems are thus coupled. This coupling is briefly covered below and further details can be found in [21].

In this coupling, the two simulation codes are kept untouched. Instead of mixing the two to obtain a third one, a weak coupling is implemented. Both codes run separately and communicate during synchronization steps with a master-slave relation. This interaction is ruled by the flow solver as it has the highest computational cost. Communication between the two solvers works as follows: at time t, the aerodynamic forces are computed by the flow solver and sent to ROBOTRAN that updates the dynamics data, the positions $\mathbf{q}$ and velocities $\dot{\mathbf{q}}$ of the lifting lines are then sent back to the flow solver. With this information, the flow solver knows where to shed the blade induced vorticity in the flow. This information exchange is executed several times during a flow solver time step using substeps for more accuracy.

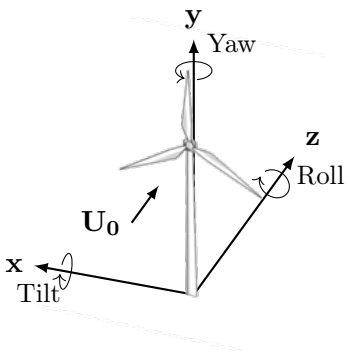

Figure 2.2: *VPM* reference frame axes conventions.

To ensure a good communication between the two codes, they must use the same reference frame. *VPM* has a particular reference frame that slightly differs from the ones generally used for this kind of simulations. The different axes and rotations are depicted in Figure 2.2. In *VPM*, the streamwise direction corresponds to the z-axis, the lateral horizontal direction corresponds to the x-axis and the vertical direction is along the y-axis. It forms a conventional right-handed

reference frame. The rotations are defined accordingly, with the right-hand rule. The yaw is positive counter-clockwise, viewed from the top. The tilt is positive clockwise seen from the right, in the positive x-direction. And the roll is positive counter-clockwise, looking downstream in the positive z-direction. These conventions will be used in all the following discussions.

2.4 Modelled wind turbine and associated controllers

The wind turbine used for the purpose of this Master's Thesis is the NREL offshore 5-MW baseline wind turbine defined in [22]. The NREL 5-MW is a three-bladed wind turbine and its main characteristics are presented in Table 2.1.

Rated power	5 MW
Rotor and hub diameter	126 m, 3 m
Hub height	90 m
Cut-in, rated and cut-out wind speed	3 m/s, 11.4 m/s, 25 m/s
Cut-in and rated rotor speed	6.9 rpm, 12.1 rpm
Optimal tip-speed ratio	7.55

Table 2.1: Main wind turbine characteristics [22].

The remaining of this section discusses the baseline controller used in this work. An Individual Pitch Control (IPC) that can be added on the top of the baseline controller is also addressed.

2.4.1 Baseline variable-speed variable-pitch controller

Any wind turbine needs to be given a control for two main reasons. They have to extract the maximum energy from the wind and stay in rated operation range to avoid being damaged. The NREL 5-MW baseline wind turbine is described with a proposed control strategy in [22]. This is the one used for this work and it will be summarized hereafter.

The NREL 5-MW controller is a variable-speed, variable blade-pitch control. It thus features two basic control systems: a generator-torque controller and a full-span rotor-collective blade-pitch controller. The generator-torque controller aims at maximizing the power capture in below-rated operation and the blade-pitch controller regulates the generator speed in above-rated operation of the turbine. They rely on two independent control loops.

Both control loops take the generator speed measurement as input data. To avoid high-frequency excitation, this information is filtered with a low-pass filter. The corner frequency is set to one-quarter of the blade first edgewise natural frequency, 0.25 Hz.

Generator-torque controller

The generator torque is computed as a tabulated function of the filtered generator speed for each of the five control regions: 1, $1\frac{1}{2}$, 2, $2\frac{1}{2}$, 3. Region 1 is the region before the cut-in wind speed where there is no torque at the generator and no power extraction. The wind is used to accelerate the rotor at start-up. Region 2 is a control region where the power extraction is optimized by targeting the optimal tip-speed ratio, maintaining it constant. In Region 3, it is the generator power that is held constant. The generator torque is thus inversely proportional to the rotor speed. The $\frac{1}{2}$ regions are linear transitions between the other regions.

A conditional statement is set on the generator-torque controller so that the torque is computed as if it were in Region 3, regardless of the generator speed, whenever the previous blade-pitch-angle command was 1° or greater to improve the output power quality at the expense of short-term overloading. This excessive overloading is avoided by saturating the torque 10% above its rated value. A torque rate limit is also implemented.

Blade-pitch controller

In Region 3, the generator speed is controlled through the aerodynamic torque which is in turn controlled by pitching the blades. This is also called Collective Pitch Control (CPC). The full-span rotor-collective blade-pitch-angle commands are computed using gain-scheduled proportional-integral (PI) control on the speed error between the filtered generator speed and the rated generator speed. The gain scheduling is based on the linearization of the relation between pitch sensitivity and blade-pitch angle. It is further described in [22] along with the detailed equations of PI control.

2.4.2 Individual pitch control

Wind turbines operating in atmospheric boundary layer experience wind speed variations across the rotor disc that result from wind shear, atmospheric turbulence and yaw misalignment. The rotating blades are thus subject to cyclically varying loads inducing fatigue. A pitch-regulated wind turbine generally having one pitch actuator per blade, the loading of each blade can thus be regulated by adjusting its angle of attack thanks to IPC. Among the possibilities proposed in [9], the implemented solution is a simple PI control taking the blades loads as input and returning differential pitch actions for each blade. IPC thus consists of a third loop action on top of the ones described before. It keeps the collective pitch control and superimposes a pitch correction for each blade.

The IPC algorithm uses the Coleman transformation to project three phases (blades) rotating system into a two axes fixed frame. The axes of this new reference frame are the direct and quadrature axes representing the lateral and the vertical direction. The projection of the blades normal bending moments in this fixed frame is computed as follows

$$\begin{pmatrix} M_{\text{tilt}} \\ M_{\text{yaw}} \end{pmatrix} = \left(\frac{2}{3}\right) \begin{pmatrix} \cos(\theta) & \cos(\theta + 2\pi/3) & \cos(\theta + 4\pi/3) \\ \sin(\theta) & \sin(\theta + 2\pi/3) & \sin(\theta + 4\pi/3) \end{pmatrix} \begin{pmatrix} M_{n,1} \\ M_{n,2} \\ M_{n,3} \end{pmatrix} \tag{2.14}$$

where θ is the rotor azimuth angular position and $M_{n,i}$ the normal bending moment of blade i. In the *VPM* reference frame, the direct axis corresponds to the x-axis and the quadrature axis to the y-axis. The obtained moments M_{tilt} and M_{yaw} are thus the moment around x and y respectively. The latter present noise and a significant 3P (three times per rotation) component. They are therefore filtered using a second-order low-pass filter at 2.5P and a notch filter at 3P. The goal of the IPC is to suppress those moments, the error is thus the moments obtained by the transformation. A PI controller is now used to evaluate the differential pitch action in the fixed frame. It is then sent back into the blades axes by the inverse Coleman transformation. Finally, the differential pitch action obtained via the IPC is superimposed to the CPC pitch angle.

Chapter 3

Static yaw misalignment

Wind turbines are not alone. In wind farms, the wake has an important effect on the successive turbines. Wake redirection is a way to address this challenge. In this chapter, wake redirection using static yaw misalignment will be investigated along with the effect of using a load reducing IPC on the yawed turbine. The first section introduces the subject and reviews some literature about what has already been done in the field. A second section addresses the methodology used and the numerical setup. Then, the obtained results are presented and analysed. Finally, a conclusion is drawn at the end of the chapter.

3.1 Introduction

With the growing number of wind farms, the knowledge of wake behaviour becomes very important. Several people have already studied wake redirection using static yaw misalignment. For example, the wake deflection for a range of yaw angles and thrust coefficients is investigated in [23], where the authors aimed at analysing the wake redirection in order to provide an analytical model to predict it. In addition, a bunch of redirection techniques are studied in [6] and the effect on the loads is also addressed. The authors studied yaw and tilt misalignment as well as individual pitch control redirection strategies. Among those presented methods, static yaw showed the greatest potential for wake steering and reduces loads in the meantime. In the context of wind farms, it thus presents a potential to increase the gathered energy by downstream turbines. In the light of this, we study static yaw in what follows.

As already mentioned in the previous chapter, IPC can be declined in a simple control algorithm that allows the mitigation of the loads. Its efficiency is underlined in [9] and a lot of studies have been done in the field with the development of more advanced controllers [24, 25]. However, only few studies treat the combination of both static yaw misalignment and load-reducing IPC. To the author's knowledge, the only article mentioning that is [10], where many aspects are addressed. This paper gives physical explanations on the obtained results and discusses the loads, the redirection and the energy gain that occurs or not in the wake by combining the two methods. They concluded that orientation (positive or negative, cf. 2.3) of the misalignment influences the physics of the flow. A positive yaw orientation is more advantageous than a negative one. Furthermore, positive yaw combined with IPC could increase both the power produced by the concerned turbine and by a downstream turbine.

The goal of this chapter is to carry out a similar study. Static yaw is thus analysed with and without IPC, focusing on the power produced, the loads suffered by the turbine and the available power in the wake. The wake characteristics are also analysed.

3.2 Methodology and numerical setup

This section firstly presents the different cases considered and describes the algorithm used to compute the wake characteristics. Secondly, the simulation setup and the different parameters are addressed.

3.2.1 Methodology

To study the impact of static yaw misalignment, several cases are considered. The different quantities studied are the power produced, the loads and the available power downstream of the wind turbine. They are studied for yaw misalignment angles from $-30°$ to $30°$ by steps of $10°$. The quantification of the fatigue loading is evaluated with Damage Equivalent Loading (DEL) [26] and relies on rainflow counting [27]. The wake characteristics such as the redirection, the meandering amplitude and wavelength are also considered. They are computed with the wake tracking algorithm described below. The effect of the IPC on the wake and the turbine is then addressed by adding IPC. All the cases are thus run without and then with IPC, totalling 14 cases.

Wake tracking algorithm

The wake tracking algorithm is based on the experimental wake tracking algorithm used in [28]. It is based on a 3D convolution between the power in a 2D plane and a 2D Gaussian function. The algorithm is used to track the wake centerline at hub height. First, the 2D streamwise velocity field at hub height is extracted. It is shown in Figure 3.1.

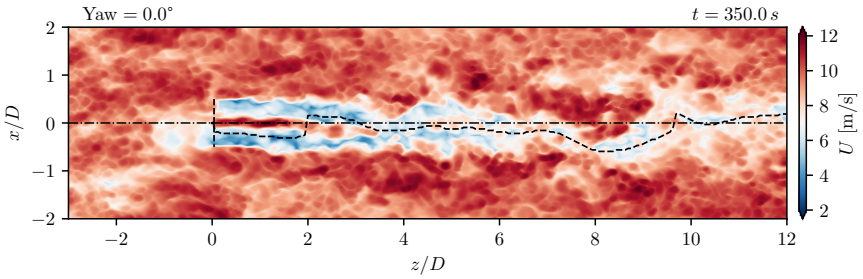

Figure 3.1: Streamwise velocity field in a horizontal plane at hub height with the wake centerline (black-dashed).

Second, the available power density is computed

$$p = \frac{1}{2} u_z \left|\mathbf{u}\right|^2. \tag{3.1}$$

Then it is convoluted with the Gaussian function

$$f_{G_{2D_{hp}}}(x, z) = A \exp\left(-\left(\frac{x^2}{2\sigma_x^2} + \frac{z^2}{2\sigma_z^2}\right)\right), \tag{3.2}$$

where $A = -1$ and $\sigma_x = \sigma_z = D/4$. It gives Figure 3.2a. The wake centroid x_c is then located by searching for the maximum of the convolution field for each downstream location (Figure 3.2b)

$$x_c = \text{argmax}\left(p_{G_{2D_{hp}}} * f_{G_{2D_{hp}}}\right). \tag{3.3}$$

This low complexity algorithm is aimed to be used in data post-processing. Yet it gives good results as it is observed in Figure 3.1. The absence of blades at the hub location creates a high-velocity zone just behind the wind turbine. This high-velocity zone disturbs the tracking. The

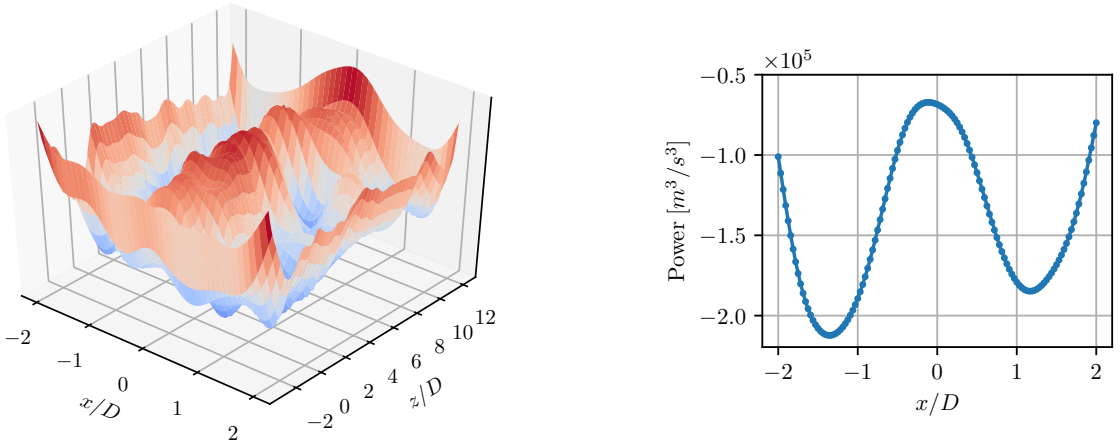

(a) 3D convolution

(b) Slice in the 3D convolution

Figure 3.2: Convolution of the streamwise power density with a Gaussian in a 2D plane at hub height (a). Slice in the convolution at 5 diameters downstream (b), where the wake centroid is tracked.

results will thus be considered starting from 3D.

The centerline position then enables to determine the wake meandering amplitudes and wavelengths. Again the method used is the one from [28]. Each wake centerline is low-pass filtered spatially with a cut-off length $L_{\text{cut-off}} = 1D$. Then the amplitudes of the wake meandering are computed as half the cross-flow distance between two consecutive maxima or two consecutive minima. The wavelengths are computed as the streamwise distance between two consecutive extrema. The downstream position of these quantities is set to the intermediate position of the two points involved in the computation. It is represented in Figure 3.3. The quantities are then binned, with respect to the downwind distance from the rotor, into half-diameter bins and the mean values are computed. With this method only the results for downstream positions from 3D to 9D are exploitable.

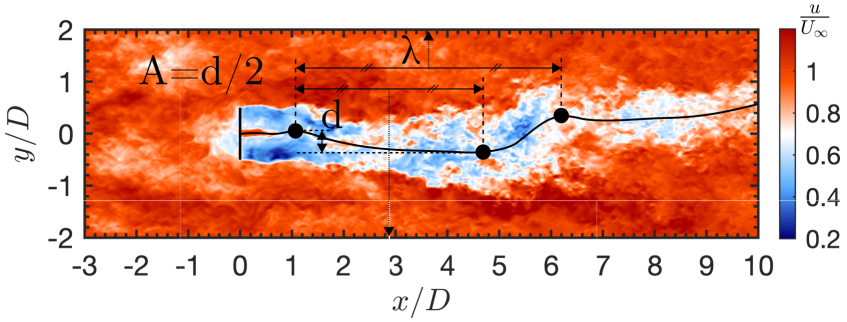

Figure 3.3: Schematic of the conventions used for the determination of the amplitudes and the wavelengths of the wake centerline oscillations [28].

3.2.2 Numerical setup

This study is carried out with numerical simulations using the LES code *VPM* (cf. 2.1) and ROBOTRAN as multibody solver (cf. 2.2). The simulations are performed for an isolated NREL-5MW wind turbine. Only the blades of the turbine are modelled with immersed lifting lines. The resolution is 32 points per diameter in every direction. The domain is depicted in Figure

3.4a. Its width, height and length are $4D \times 3D \times 15D$ and the flow is unbounded in the x and z directions. The turbine is located at the centre of the domain 3 diameters downstream of its entry. The inflow has a streamwise wind speed at hub height $\mathbf{U_0} = 9\,\mathrm{m/s}$. The turbine is thus working in Region 2 at optimal tip-speed ratio. The wind shear coefficient α is 0.2 in Equations 2.10 and 2.11. For the turbulent cases, the turbulence intensity is 10% and is synthesized with a Mann box [18] that is 32-diameters long. The time step is constant and the CFL number is between 0.12 and 0.46. The flow is studied after it develops for 20 convective times (4/3 of through-flow). The different quantities are studied during one through-flow the twelve diameters downstream of the turbine (12 convective times) for the cases without turbulence and during one Mann box through-flow (32 convective times) for turbulent cases.

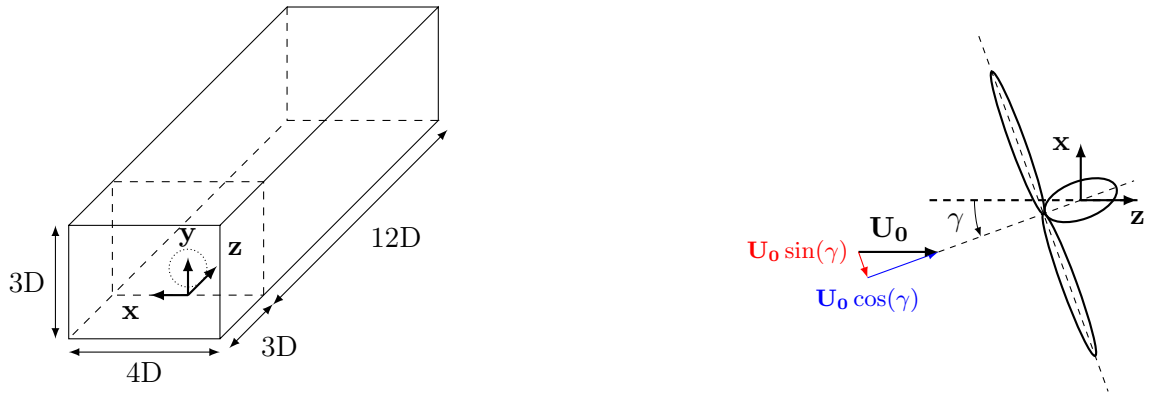

(a) **(b)**

Figure 3.4: Computational domain with its dimensions (a) and the wind turbine showing the positive orientation convention of the yaw angle γ, with the inflow velocity projected in the wind turbine frame (b).

3.3 Results

This section presents the results obtained. First, cases without turbulence are presented. They are used to explain some physics that lies behind the observed results. Then the results for the turbulent cases are presented. The orientation (positive or negative) of the yaw angle will have an impact on the physics and the reader should thus be aware of the orientation convention used as depicted in Figure 3.4b.

3.3.1 Sheared inflow

This subsection begins with some explanations about the aerodynamics of the inflow with the turbine blades to explain the loading. The impact of the shear and the misalignment angle are thus discussed. The loads for the different misalignment angle are then presented. Next, the addition of the IPC is tackled. And finally, the impact on the power produced and on the power available downstream is addressed.

Let us first consider the effect of the shear with the cases drawn in Figure 3.5a-c. The shear is a major stakeholder in the fatigue loading of a wind turbine. It causes variation of the inflow velocity across the rotor disc. The inflow has a higher velocity at the top and a lower one at the bottom. Hence, the shear creates an up/down imbalance. When a blade passes on the top side, it thus experiences a higher inflow velocity. As depicted in case (b), it results in a higher relative velocity $\mathbf{W}$ encountered by the blade and a higher angle of attack. The loading is thus even bigger. When the blade is at the bottom, the inflow velocity is lower and so are the relative

velocity and angle of attack as depicted by (c). Then, the lift and thus the loading are smaller. The extreme blade positions being $\theta = 0$ and $\theta = \pi$ it explains the extrema of the flapwise bending moment for a yaw angle $\gamma = 0°$ in Figure 3.6.

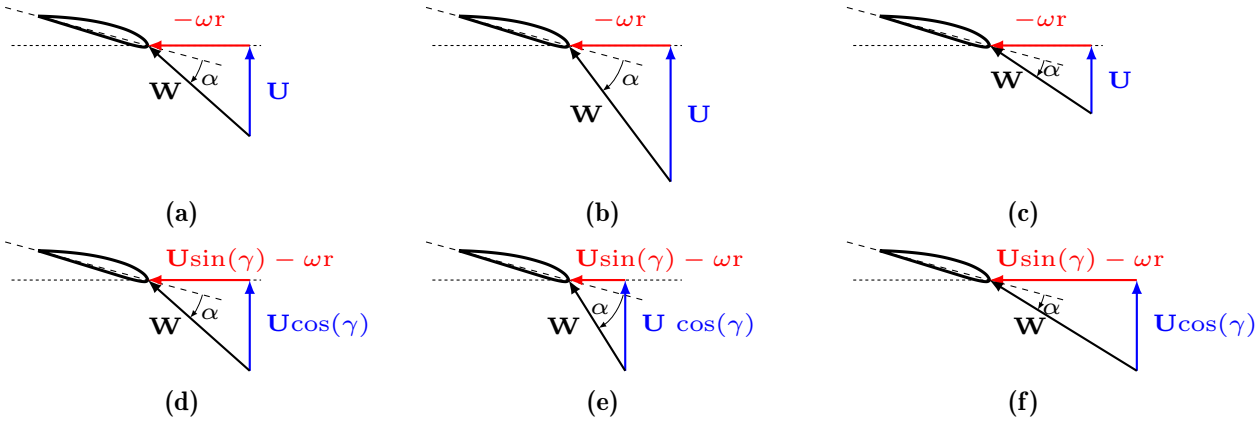

Figure 3.5: Velocity triangles for different positions and orientations with respect to the inflow. The first line underlines the effect of the shear where the base case (a) is compared to a higher inflow velocity (b) and a lower inflow velocity (c). The second line highlights the impact of the yaw angle and compares the base case (d) to cases where the tangential component of the inflow is in the same direction (e) or against (f) the blade rotation. **U** is the streamwise velocity, ω the rotational speed of the blade, **W** is the relative speed with respect to the airfoil, α is the angle of attack and γ is the yaw misalignment angle.

When considering the effect of the yaw, the inflow velocity breaks up into a tangential and a normal component in the rotor frame as in Figure 3.4b. The blade rotation is not fully perpendicular to the wind inflow velocity anymore. Therefore, the effect of the tangential component adds to the effect of the blade rotation velocity (Figure 3.5d-f). The blades rotate clockwise. If the turbine is yawed positively, the blade tends to rotate in the same direction as the wind at the top ($U\sin(\gamma)$ has the same direction as the blade rotation). The tangential component of the inflow velocity and the rotational speed of the blade thus balance each other and corresponds to case (e) in Figure 3.5. Because of that, the relative velocity **W** is lower and the angle of attack higher. But when the blade is at the bottom, the tangential component of the inflow is against the blade rotation. Contributions from both the blade rotational speed and inflow tangential component add. It results in a higher relative velocity while the angle of attack is lower, as in case (f).

The relative velocity and angle of attack then influence the loading of the blade through lift and drag forces. To understand how it affects the blade solicitations, consider the lift and drag equations

$$\mathbf{L} = \frac{1}{2}\rho \mathbf{W}^2 c_l A, \tag{3.4}$$

$$\mathbf{D} = \frac{1}{2}\rho \mathbf{W}^2 c_d A, \tag{3.5}$$

$$c_l = f(\alpha, ...) \propto \alpha \qquad \text{for } \alpha \ll, \tag{3.6}$$

$$c_d = f(\alpha, ...) \approx Cst \qquad \text{for } \alpha \ll, \tag{3.7}$$

where ρ is the fluid density, A the blade area, α the angle of attack, and c_l and c_d are the lift and drag coefficient respectively. The contribution of the velocity is dominant compared to the angle of attack in term of applied force to the blade. Indeed, the angle of attack only intervenes in the lift equation (through c_l) while the relative velocity comes to the square in both lift and

drag equations. The effect of the wind shear, described above, thus tends to increase the loading at the top and decrease it at the bottom whereas it is the opposite for positive yaw. Both thus counteract each other as summarized in Table 3.1 and mitigate the fatigue loading.

	Top ($\theta = 0$)	**Bottom** ($\theta = \pi$)
Shear	**W** $\uparrow$, $\alpha \uparrow \Rightarrow$ L $\uparrow$	**W** $\downarrow$, $\alpha \downarrow \Rightarrow$ L $\downarrow$
Positive yaw	**W** $\downarrow$, $\alpha \uparrow \Rightarrow$ L $\downarrow$	**W** $\uparrow$, $\alpha \downarrow \Rightarrow$ L $\uparrow$
Negative yaw	**W** $\uparrow$, $\alpha \downarrow \Rightarrow$ L $\uparrow$	**W** $\downarrow$, $\alpha \uparrow \Rightarrow$ L $\downarrow$

Table 3.1: Effect of shear and yaw misalignment on the blades solicitations.

If the yaw angle is negative it is the opposite, the blade tends to rotate in the opposite direction as the wind at the top and in the same direction at the bottom. The tangential component of the relative velocity with respect to the blade **W** is higher at the top and lower at the bottom. It corresponds to cases (f) and (e) respectively. Both shear and yaw then make the relative velocity higher at the top and lower at the bottom. It results in even higher solicitation imbalances and an increase of the fatigue loading. Yaw misalignment thus adds a contribution to the up/down imbalance caused by the shear, either increasing or decreasing it.

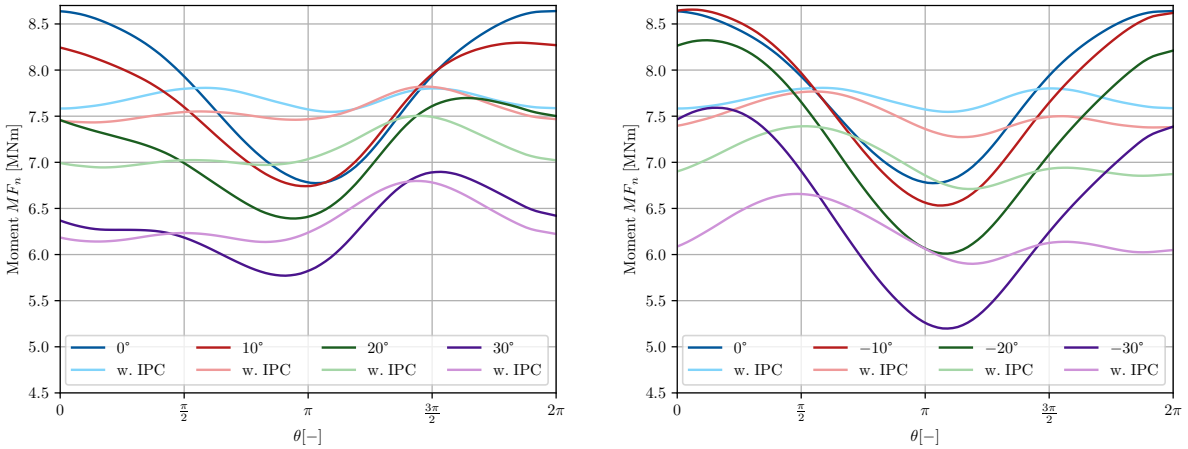

(a) Positive yaw

(b) Negative yaw

Figure 3.6: Azimuthal evolution of the blades flapwise bending moment for positive (a) and negative (b) yaw misalignment angles. Darker and lighter colours stand for the use of the IPC or not, respectively.

Let us now look at the mean azimuthal evolution of the blade flapwise bending moment presented in Figure 3.6. The extrema are mainly located where the effect of the shear is maximum and minimum. For both positive and negative static yaw misalignment, the mean value of the loads decreases with the misalignment. It is caused by the lower normal inflow velocity due to its projection in the turbine frame. However, the amplitude decreases in the case of positive yaw angles and increases for negative angles. Indeed, as explained with the velocity triangles, positive yaw orientation counteracts the effect of the shear while negative orientation exacerbates the induced imbalance. The comparison in term of DEL is given in Figure 3.7c. The equivalent fatigue loading is decreased for positive yaw angles and increased for negative yaw angles.

The shape of the cycle changes especially for positive yaw. As explained previously, the imbalance is reduced in positive yaw due to the combination of the tangential inflow velocity component

and the blade rotation. At the top, the blade rotation and the tangential velocity counteracts from $\theta = \frac{3\pi}{2}$ (or $-\frac{\pi}{2}$) to $\theta = \frac{\pi}{2}$ where they are in the same direction. This effect is maximum at $\theta = 0$ (or 2π) where the blade rotational velocity is fully horizontal and in the same direction as the inflow tangential velocity. The reduction in loading at $\theta = 0$ eventually surpasses the other positions and induces a shift of the maximum. The maximum is shifted to the position where the reduction has the lowest impact, that is $\theta = \frac{3\pi}{2}$. At this position, the blade rotational velocity is fully vertical and do not interact with the tangential component of the inflow. By contrast, in negative yaw the extrema stay at the same position because the imbalance is increased. The effect of the IPC is clearly visible in Figure 3.6. The oscillations are nearly totally damped and the fatigue loading is decreased by a lot for IPC cases, as can be seen in Figure 3.7c. However, IPC seems to be less efficient as the yaw angle increases.

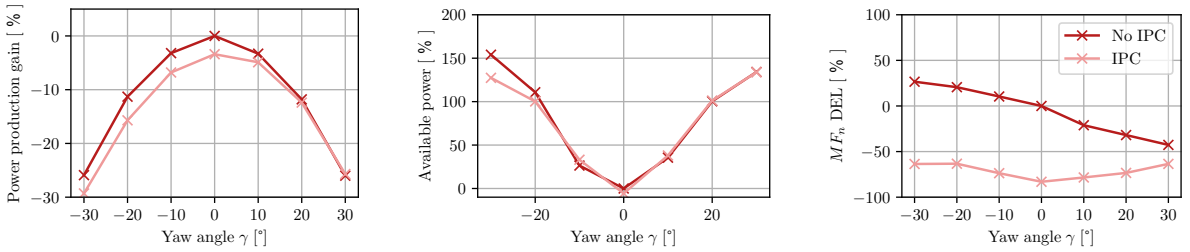

(a) Produced power **(b)** Power downstream **(c)** flapwise bending moment

Figure 3.7: Changes in produced power (a), power available in the wake 7D downstream (b) and flapwise bending moment damage equivalent loading (c) with respect to the yaw angle, with and without IPC. The comparisons are expressed in relative percent compared to the 0° without IPC case. Darker and lighter colours stand for the use of the IPC or not, respectively.

We now look at the impact of IPC on the downstream velocity field. Since there is no turbulence in those cases, IPC mainly must mitigate the imbalance due to the shear in the inflow. The effect of IPC is thus to decrease the angle of attack and hence decrease the gathered power at the top, and the reverse at the bottom. As less power is extracted at the top and more at the bottom, the flow velocity after the rotor using IPC is higher at the top and lower at the bottom, as depicted in Figure 3.8. IPC generates an excessively low loading at the top and an excessively high one at the bottom. It results in a deviation from the optimal induction which translates in a general power loss when using IPC. One can note from Figure 3.7a that the relative loss is lower in the case of positive yaw. Actually, it already contributes to the mitigation of the imbalance, allowing a lower contribution of IPC, while the opposite can be concluded for negative yaw.

The higher and lower velocity zones created by IPC we just mentioned also have an impact on the power that flows downstream. When we look from downstream to upstream, the wake rotates clockwise as the flow goes downstream. The gain in velocity at the top and the loss at the bottom induced using IPC also rotates. They end up at the right and at the left of the wake, respectively, for a certain position downstream. It is observable in Figure 3.9 at 7 diameters downstream. When positive yaw misalignment is added, the wake is shifted to the left. Considering the location that would potentially be occupied by a second wind turbine (in dashed in Figure 3.9), the low-velocity zone is pushed away while the high-velocity one is pulled in. It thus has the potential to profit from this velocity gain and to increase the available power downstream for a second wind turbine. On the contrary, negative yaw tends to pull the velocity deficit at the downstream turbine location and push the high velocity away. It is observable at 7 diameters downstream.

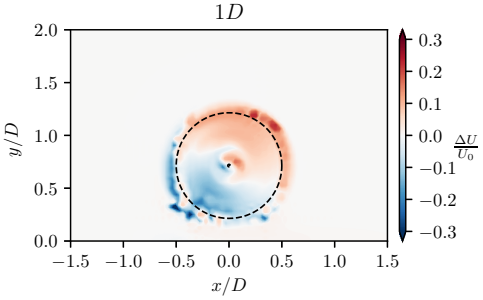

Figure 3.8: Difference in wake mean streamwise velocity at 1D downstream the rotor for $\gamma = 0°$ when IPC is added. The rotor plane is viewed from downstream. The dashed circle represents the position of the rotor of an aligned wind turbine located downstream.

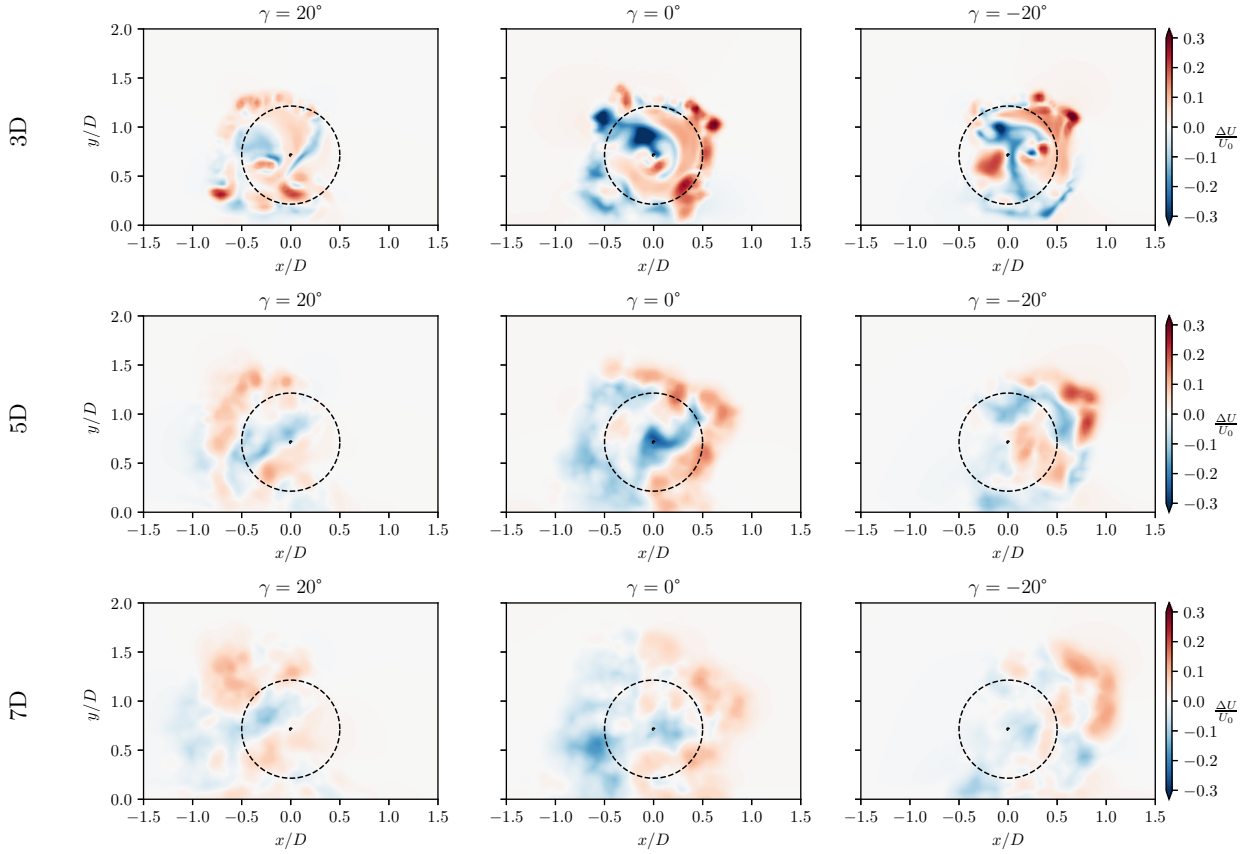

Figure 3.9: Difference in wake mean streamwise velocity for different downstream positions and yaw angles when IPC is added. The rotor planes are viewed from downstream. The dashed circle represents the position of the rotor of an aligned wind turbine located downstream.

The power available is evaluated by taking the mean power available in the area that would be occupied by a downstream turbine. From Figure 3.7b, the introduction of a misalignment angle increases the available power downstream by redirecting the wake. The introduction of IPC slightly increases the power available in the wake for moderate positive yaw misalignment. However, IPC is more prone to decrease the available power downstream when it is used with negative yaw, as stated above.

3.3.2 Turbulent sheared inflow

In the last subsection, cases without turbulence were presented. It helped to understand the impact of the yaw misalignment combined with the shear. Now, to have more realistic quantifications on the phenomena described earlier, turbulent cases are studied. The turbulent intensity is 10% which is a standard value for onshore wind turbines. Again, we discuss the differences observed for the different misalignment angles. To the quantities previously studied that are the power produced, the blade flapwise bending moment and the available power downstream, we add the tangential blade bending moment and the yaw and tilt moments. At the end of the section, wake behaviour is also discussed.

The loading cycles for a turbulent inflow vary drastically from one rotation to another, unlike for the non-turbulent case. This is caused by the turbulence, making the inflow vary continuously. Indeed, in the previous cases, only the effect of shear and yaw misalignment contributed to the inflow differences across the rotor disc. Now the effect of those varying turbulent structures, varying in both space and time, is added. Again, mean cycles of flapwise bending moment are drawn in Figure 3.10. The same observations from the non-turbulent cases hold: lower mean values when the misalignment increases, but lower and higher amplitudes for positive and negative angle respectively. The variation with the yaw angle is given in term of DEL in Figure 3.11b.

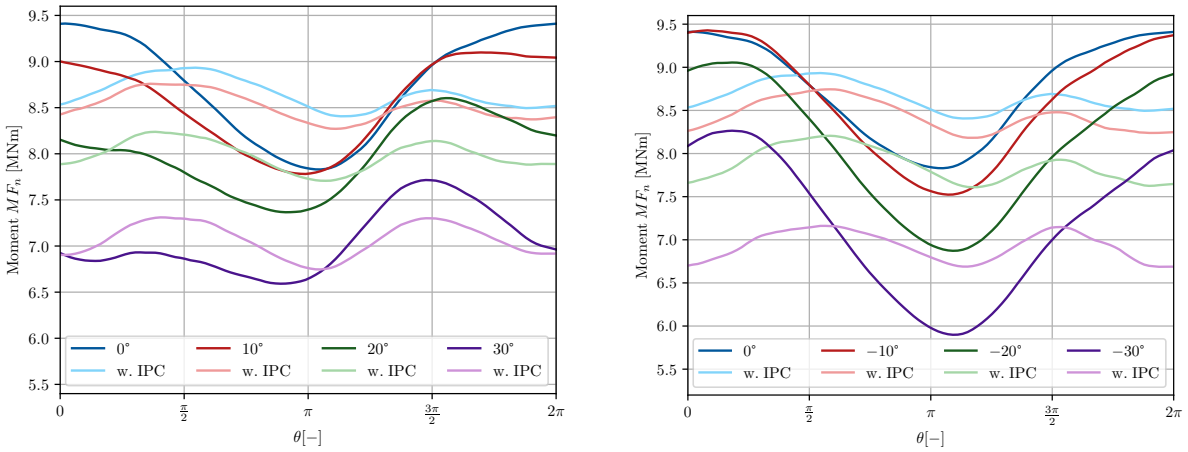

(a) Positive yaw

(b) Negative yaw

Figure 3.10: Azimuthal evolution of the blades flapwise bending moment for positive (a) and negative (b) yaw misalignment angles, in a turbulent inflow. Darker and lighter colours stand for the use of the IPC or not, respectively.

Positive yaw decreases the blade flapwise fatigue loading while negative yaw increases it. The load increase in negative yaw seems to have a maximum around $\gamma = -20°$, then it starts to decrease back. When IPC is added, the load oscillations are significantly reduced. The loads mean cycles in Figure 3.10 are largely flattened. The DEL curve with IPC is more symmetrical around 0° than without IPC.

Another type of loading encountered is the tangential moment experienced by the blades. It is actually the torque applied to the shaft of the wind turbine, responsible for the power production. However, its variations cause fatigue on the shaft. The DEL of the blades tangential moment is displayed in Figure 3.11e. Unlike the blade flapwise bending moment, it is lower for negative yaw than for positive yaw. IPC helps to reduce it but is not as efficient as for the blade flapwise bending moment. Indeed, the IPC inputs are the yaw and tilt moments that are caused by the

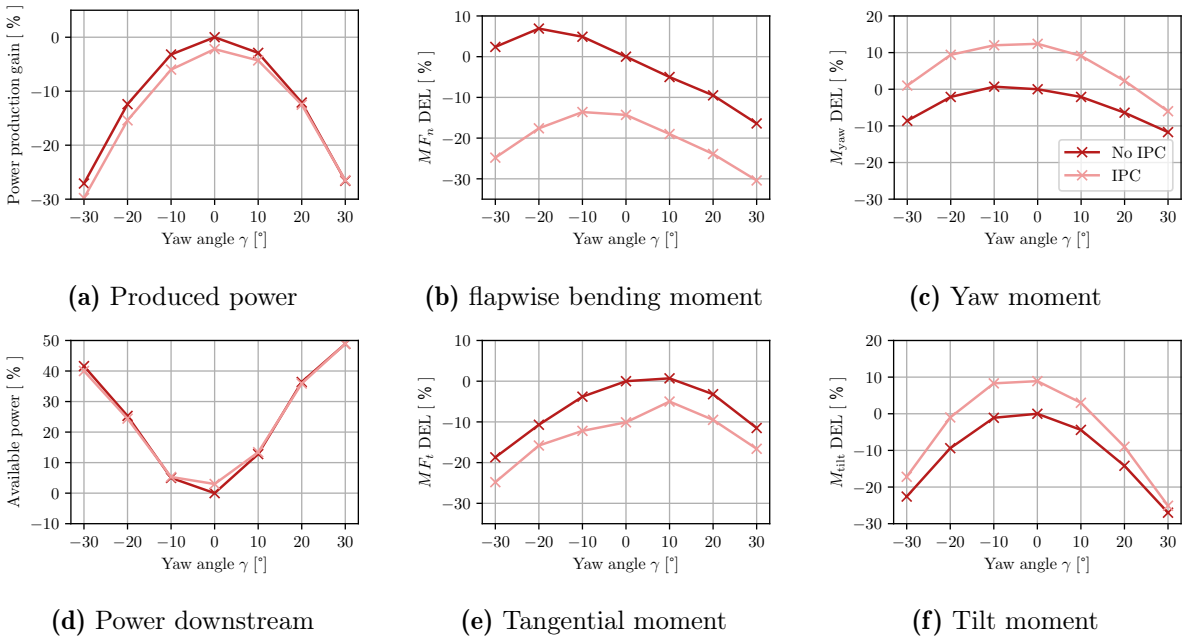

(a) Produced power **(b)** flapwise bending moment **(c)** Yaw moment

(d) Power downstream **(e)** Tangential moment **(f)** Tilt moment

Figure 3.11: Changes in produced power (a), power available in the wake 7D downstream (d), blade flapwise bending moment damage equivalent loading (b), tangential bending moment damage equivalent loading (e), yaw moment damage equivalent loading (c) and tilt moment damage equivalent loading (f) with respect to the yaw angle, with and without IPC. The comparisons are expressed in relative percent compared to the 0° without IPC case. Darker and lighter colours stand for the use of the IPC or not, respectively.

blade flapwise bending moment. By design, the goal of IPC is thus not to mitigate the fatigue of the tangential moment. Hence, it is nice IPC also helps in this case.

The next type of loading is the yaw moment. It applies to the yaw bearings of the yaw mechanism that control the wind turbine orientation with respect to the wind. Both with the tilt moment that will further be discussed, they are induced by the blade flapwise bending moment. The yaw moment comes from a left/right solicitation imbalance of the rotor. It corresponds to an imbalance between the $]0;\pi[$ and $]\pi;2\pi[$ azimuthal sectors, where the bounds are neutral positions for the left/right imbalances. The more the blade flapwise bending moment is symmetrical around π, the smaller the yaw moment. From Figure 3.11c, both yaw orientations tend to reduce the yaw moment. The positive orientation is more effective at this reduction.

The last type of loading discussed is the tilt moment. It mainly applies to the tower and its connection to the nacelle. Like the yaw moment, it is induced by the blade flapwise bending moment but is due to top/bottom imbalances. That is to say imbalances between the $]-\frac{\pi}{2};\frac{\pi}{2}[$ and $]\frac{\pi}{2};\frac{3\pi}{2}[$ azimuthal sectors. It is thus mainly caused by shear. Again it decreases with the misalignment, as depicted in 3.11f. However, it is lower for positive yaw angles. It is due to the displacement of the maximum that moves away from 2π where it has the most impact. In addition, the amplitude increases for negative yaw which tends to increase the imbalance.

For tilt and yaw moments IPC increases the DEL. In fact, IPC well contributes to loads reduction. It mainly acts on low frequency (lower than 1P) variations of the loading. However, the DEL quantification is more sensitive to high frequency (3P and more) that are not reduced by IPC. IPC even tends to slightly increase high frequencies. Therefore, the DEL with IPC can be higher than without. More comments on that are made in the next chapter and Appendix C.

The power produced for yawed cases without IPC does not really differ for positive or negative angles. Whatever the direction of the misalignment, the projection of the inflow perpendicularly to the turbine is the same. The introduction of IPC induces a power loss. For positive yaw, the difference in power due to IPC disappears as the misalignment becomes more important. Here, a little gap appears between positive and negative angles. The power produced with IPC for negative angles is lower. As explained previously, IPC is more solicited for negative yaw and hence leads to larger power losses.

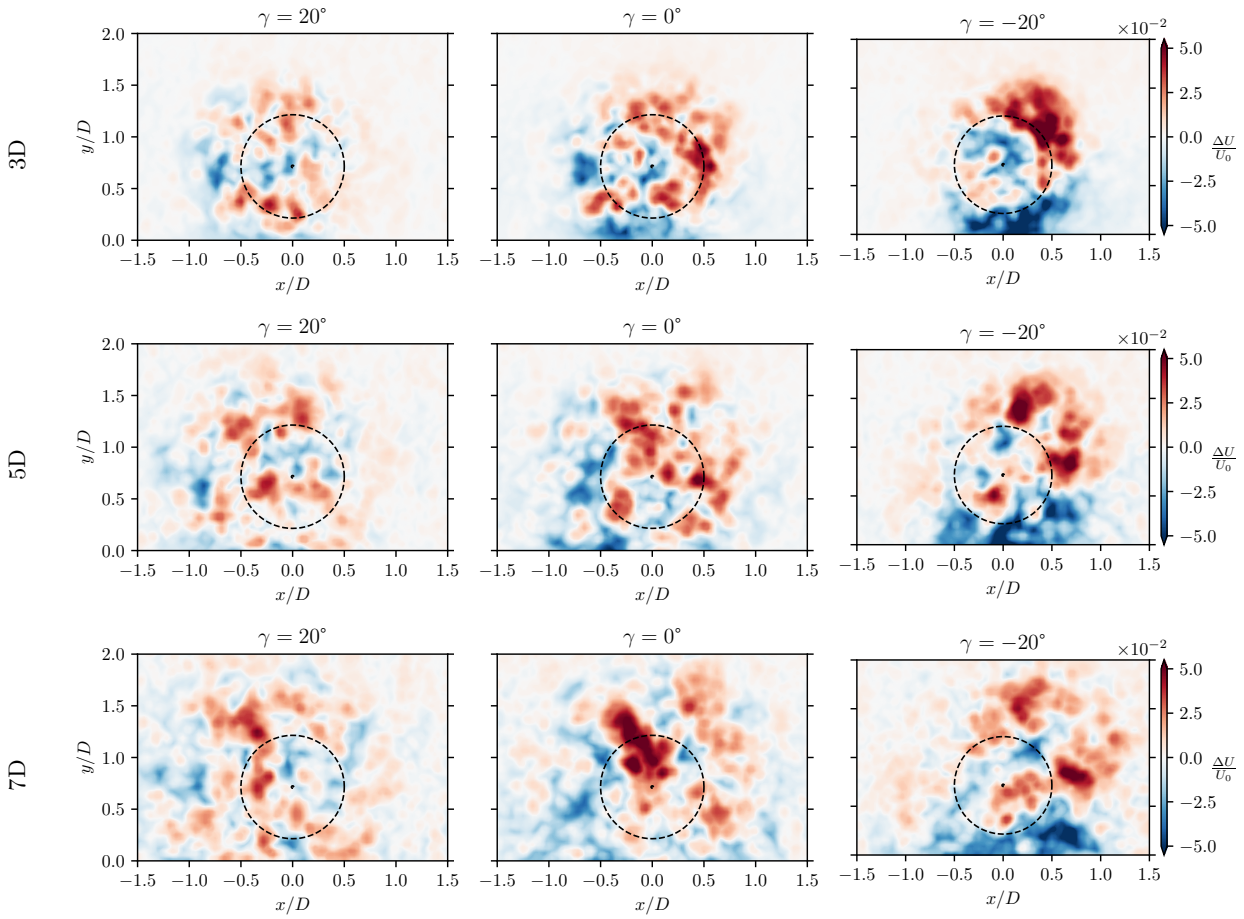

Figure 3.12: Difference in wake mean streamwise velocity for different downstream positions and yaw angles when IPC is added. The rotor planes are viewed from downstream. The dashed circle represents the position of the rotor of an aligned wind turbine located downstream.

Regarding the available power downstream, it is the positive yaw that yields the highest power gains (Figure 3.11d). It is in part due to the larger redirection provided by positive yaw as shown in [6]. It is observable in Figures 3.13 and 3.14a. IPC first introduces a power gain, for small misalignment angles. Then for larger positive angles, this gain weakens and disappears. On the contrary, for larger negative angles, the gain weakens and becomes a loss. This has been explained previously with the higher velocity at the top and lower at the bottom, that are rotated downstream and then flushed to the left or the right. It makes a downstream turbine encounter either the higher or the lower velocity zone for positive or negative yaw respectively. here, it is illustrated by the fact that a power loss in the wake appears for negative angles, due to IPC. Although it is less obvious than for the non-turbulent case, the higher and lower velocity zones can still be identified in Figure 3.12. The velocity difference is more marked for negative yaw

because IPC is more solicited. The higher velocity bubble is pushed away from the rotor location and the rotor that would lie at this location would essentially experience the low-velocity bubble. It is the opposite for positive yaw where the downstream rotor would rather experience the high-velocity bubble created by IPC. Nevertheless, it is less evident than in the no-turbulence cases as the wake is mixed in addition to the lower contribution of IPC and the gain or losses in power are really small. From Figure 3.12, let us also note the uneven velocity distribution downstream, caused by IPC. It may lead to increased loading for a downstream wind turbine.

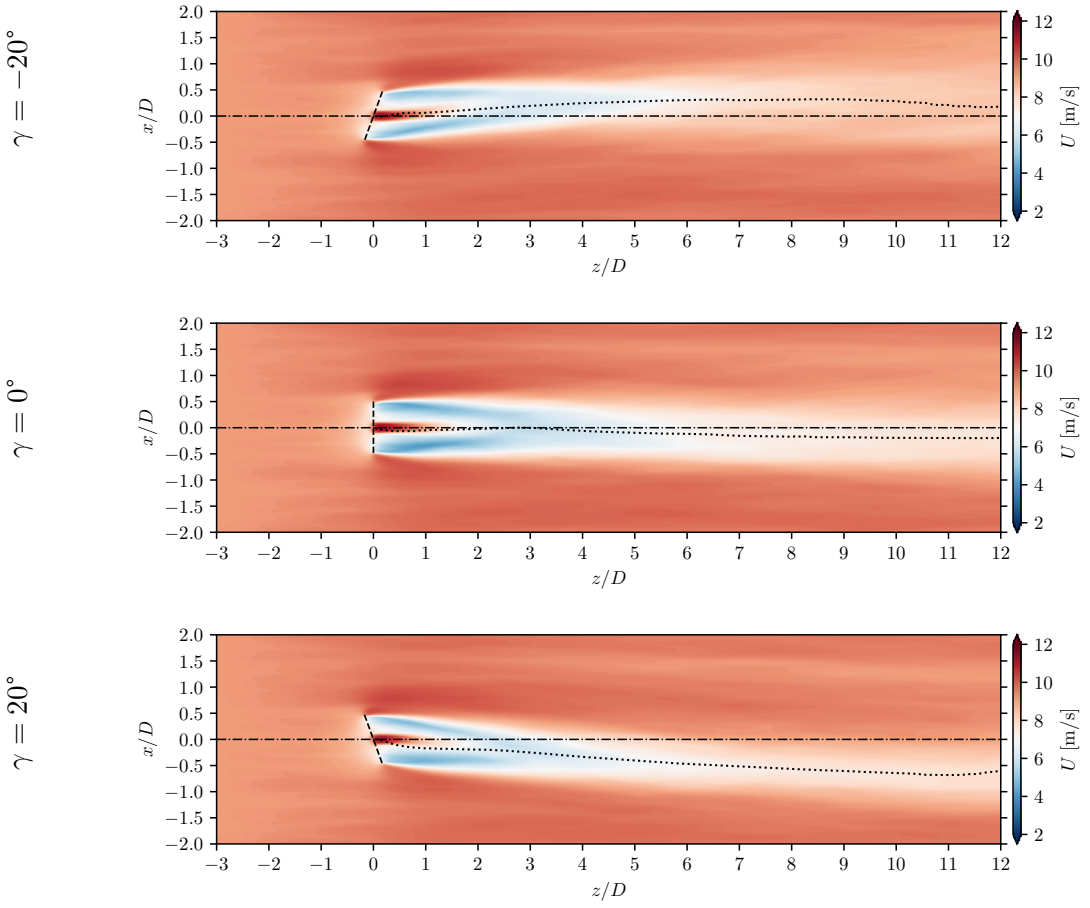

Figure 3.13: Mean streamwise velocity field in a horizontal plane at hub height with the mean wake centerline (black dashed) for different yaw angles, without IPC.

The impact of the misalignment and IPC on the wake characteristics is also briefly investigated. From Figure 3.14a, the redirection is larger for positive angles. IPC decreases the redirection for large negative angles but does not seem to have an impact on positive angles. The standard deviation of the wake centerline position is also given in Figure 3.14b. The wake meandering amplitudes and wavelengths are displayed in Figure 3.16. First looking at the amplitude, we can see that for every case the amplitude of the meandering increases with the distance from the turbine. Also, it turns out that the misalignment makes the meandering amplitude grows faster. One can note that this phenomenon is more marked for negative angles. Hence, the wake mixing is increased and the velocity deficit is lower and wider, as shown in Figure 3.15. This can be further confirmed with the standard deviation of the wake position. When the misalignment angle increases, the standard deviation increases. This increase is larger for negative angles. No real conclusion has been drawn from the wavelength. Yet, for an aligned turbine, the wavelength is rather constant with the distance from the turbine. It seems that for the misaligned case, the

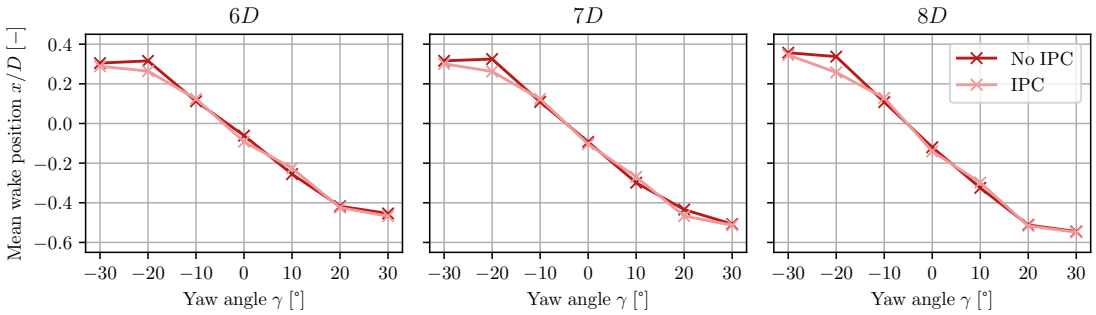

(a) Wake mean centerline position

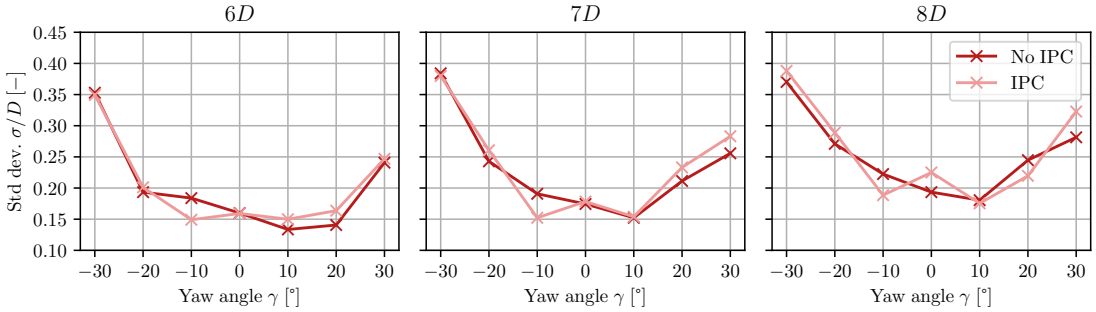

(b) Wake centerline position standard deviation

Figure 3.14: Wake mean centerline position (a) and standard deviation (b) at 6, 7 and 8 diameter downstream for the different cases. Darker and lighter colors stand for the use of the IPC or not, respectively.

wavelength is increased near the turbine and then decreases back. Except for the redirection, IPC does not seem to have any well identifiable impact on the wake meandering. Indeed, IPC seems to reduce the meandering amplitude but it is not confirmed with the standard deviation.

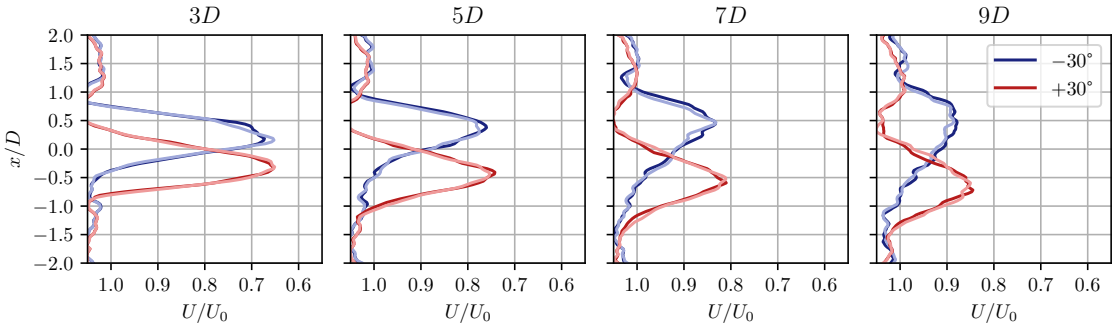

Figure 3.15: Mean velocity profile for the ±30° case for several downstream positions. Negative (blue) and positive (red) angles are plotted against each other. Darker and lighter colours stand for non-IPC and IPC cases respectively.

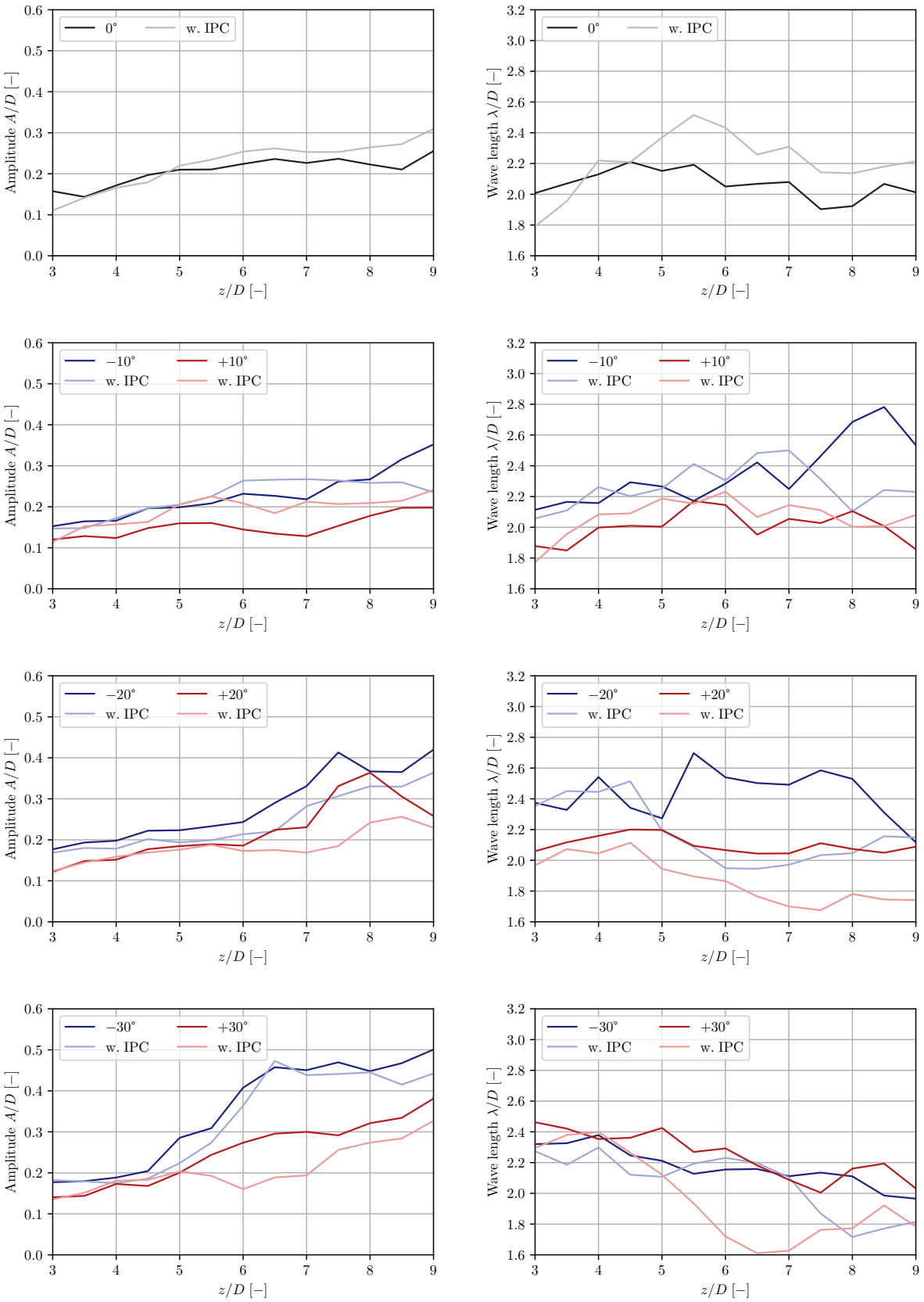

(a) Wake meandering amplitude

(b) Wake meandering wavelength

Figure 3.16: Mean binned wakes amplitudes (a) and wavelengths (b) with respect to the downstream location for the different cases. Negative (blue) and positive (red) angles are plotted against each other. Darker and lighter colours stand for the use of the IPC or not, respectively.

3.4 Conclusion

In this chapter, redirection using yaw misalignment has been studied. The goal was to maximize the power downstream and the available power and wake behaviour have thus been considered. Yaw misalignment triggers the question of the loads. We thus looked at the loads and we addressed the possibility of using load reducing IPC. The impact of the IPC has also been evaluated.

In the methodology, a simple algorithm to track the wake centerline and compute some characteristics of the wake has been described. It relies on the 3D convolution of the power in a horizontal plane at hub height with a 2D Gaussian. Despite its simplicity, it gives satisfying results and allowed to get some insights about the wake behaviour.

In the first part, static yaw cases with and without IPC were investigated with a non-turbulent inflow. It helped to understand the related mechanisms and the phenomena that lie behind the observed results. The effects of the shear and misalignment on the loads were firstly explained. It was shown that positive yaw tends to counter the imbalances in the inflow velocity experienced by the rotor, while negative yaw tends to increase it. Then the effect of IPC was addressed. When the unbalance is mainly due to shear, IPC induces a higher velocity on the top and a lower on the bottom in the wake. This can be exploited with the redirection of the wake. Positive yaw can make a downstream turbine take advantage of this highest velocity bubble that rotates clockwise with the wake.

Secondly, the same study was conducted with a turbulent inflow (TI = 10%) to provide more realistic insights into the possible advantages or drawbacks such strategies of redirection have. The first thing to keep in mind is that positive yaw beats negative yaw in many aspects. It is better regarding the power produced and the power available in the wake. Regarding the loads, positive yaw has a lower blade flapwise bending moment, yaw and tilt moment but it is slightly worst for the tangential bending moment. Nevertheless, considering the advantages it gives in terms of power and redirection, positive yaw gives more advantages. Hence, positive yaw is to prioritize as a wake steering strategy. Furthermore, considering the wake characteristics, positive yaw is more relevant as a redirection strategy as the redirection is larger and the velocity deficit thinner than for negative yaw angles. However, some interest may be found in the increased meandering in negative yaw. Then it is concluded that the use of the IPC is worth the power loss as it greatly reduces the loads. On top of that, IPC has the potential to slightly increase the power for downstream turbines when it is combined with positive yaw. Nevertheless, a more economical study should be conducted to confirm its worthiness, based on the Levelised Cost of Energy (LCOE) and a Life Cycle Assessment (LCA) for example.

When comparing to the literature, most of the observation made here are in accordance with what has already been done. The conclusion drawn here is the same: positive yaw is to be considered as an interesting redirection strategy and its combination with IPC can lead to significant load reductions.

Chapter 4

Dynamic yaw misalignment

The previous chapter was about wake redirection. In this chapter, another strategy aiming at maximizing the power for downstream turbines is presented. This strategy relies on dynamic yaw. Again, a yaw misalignment is introduced with the difference that the control is dynamic and passive. The goal is thus to let the yaw angle freely vary in time and quantify the impact it has. Such a strategy has an impact on the loads. Load reducing IPC is thus also included in the study. The first section introduces the subject. Second, the numerical setup is presented. The results are then analysed and finally some conclusions are drawn.

4.1 Introduction

This dynamic yaw strategy aims to dissipate the wake and accentuate its recovery to maximize the power downstream of a wind turbine. Wakes already naturally dissipate with the help of turbulence. On one hand, the turbulence itself causes mixing in the wake and thus participate in the recovery. On the other hand, the turbulence creates an uneven loading of the rotor that induces wake meandering. This meandering motion also actively participates to wake dissipation. The goal is to see if dynamic yaw can accentuate this meandering motion.

Studies assessing dynamic yaw are scarce. The only one found by the author concerning wind farm power optimization is [4]. In this paper, dynamic yaw strategies are investigated but the high computational cost of the control used makes it not practically implementable. Here we will thus focus on a simple dynamic passive yaw strategy that is free yaw. Free yaw is already known from small downwind wind turbines. This strategy only applies to downwind wind turbines for stability reasons. The studies about free yaw mainly treat stability, like [29, 30], and are conducted for small wind turbines. No studies about free yaw for large wind turbines nor the wake behaviour in such a configuration seems to exist and it is the subject of this chapter.

In this chapter, we aim at quantifying the possible benefits from a free yawing 5-MW wind turbine. We expect an increased wake meandering amplitude to enable more power extraction downstream. The dynamic motion of the turbine may lead to increased loads for the free yawing turbine. The impact of load reducing IPC is thus also studied.

4.2 Numerical setup

To study the effect of free yaw, a free yawing wind turbine is compared with a turbine aligned with the inflow. Both cases are also reproduced using IPC. The different quantities studied are the loads, the power produced and the power available downstream to identify the pros and cons of such strategies. In addition, the wake behaviour is analysed for the listed cases. Damage

equivalent loading is used to quantify the loads and the wake is studied using the algorithm presented in the previous chapter.

As before, the study is carried out with numerical simulations using the LES code *VPM* and the multibody solver ROBOTRAN. The same simulation parameters as for Chapter 3 are used. The simulations are also performed using the NREL-5MW wind turbine. However, in the context of free yaw, it has been turned into a downwind configuration. The downwind configuration is more stable for free yaw as shown in [30]. The only thing that changed is the shaft overhang that is oriented downstream. Similar configurations of the NREL-5MW are found in [31, 32, 33]. No blade coning nor nacelle tilt are considered and only the blades of the turbines are modelled with immersed lifting lines. The resolution is 32 points per diameter in every direction. The domain is the same as the one depicted in Figure 3.4a. Its width, height and length are $4D \times 3D \times 15D$ and the flow is unbounded in the x and z directions. The turbine is located at the centre of the domain 3 diameters downstream of its entry. The inflow has a streamwise wind speed at hub height $\mathbf{U_0} = 9\,\mathrm{m/s}$. The turbine is thus working in Region 2 at optimal tip-speed ratio. The wind shear coefficient α is 0.2. A turbulent inflow is synthesized with a Mann box [18] that is 32-diameters long. The time step is constant and the CFL number is between 0.12 and 0.46. The flow is studied after it develops for 20 convective times (4/3 of through-flow) and the different quantities are studied during one Mann box through-flow (32 convective times).

4.3 Results

This section presents the different results obtained while studying free yawing and IPC. The section begins by focusing on the loads the turbine experiences. Each type of load is addressed, with the effect of free yaw and IPC. A quantification in term of DEL is used. Then the focus is on power. First, the difference in power production is discussed. Secondly, we talk about the wake and the power it contains for downstream turbines.

The first thing we look at is the evolution of the yaw angle and yaw rate. A turbine should stay aligned as much as possible with the inflow to ensure a fair power production. The yaw rate is a design parameter for the yaw bearings and should not be too high. Moreover, a too fast yaw rate can create a large gyroscopic moment that would damage the turbine. From Figure 4.1a, one can see that the free yawing turbine is stable and stays in reasonable bounds for the yaw angle. The yaw rate is plotted in Figure 4.1b, where it has been filtered for the sake of being readable. It is also bounded and never excess $2\,^\circ/\mathrm{s}$ when not filtered. To make some comparison, the nominal yaw rate of the actuator is $0.3\,^\circ/\mathrm{s}$. However, other studies on dynamic yaw for multi-megawatts wind turbines used yaw rates about a few degrees per second. In [34], the aerodynamics of wind turbines is studied for yaw rate up to $3\,^\circ/\mathrm{s}$. Also, [4] investigated yaw controls with yaw rates up to $5\,^\circ/\mathrm{s}$. The yaw rates we obtain thus seems still really acceptable. Another simulation with another longer Mann's box has also been examined to confirm those results and it shows similar results. It is joined in Appendix B. Given the yaw angle variation we have here, this dynamic yaw strategy is indeed more a dissipation than a redirection strategy.

The first effect of IPC is already observable here. When the free yawing turbine is provided with IPC, the yaw angle variations are weakened. In fact, the changes of orientation of the rotor are caused by rotor force imbalances. Hence it is reduced with the IPC as it aims to reduce loads imbalances.

Now we will focus on the loads. Let us begin with the flapwise bending moment represented in Figure 4.2a. The effect of freeing the yaw degree of freedom does not reduce its amplitude

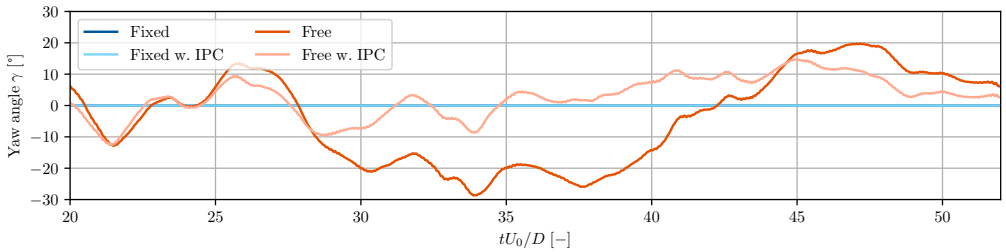

(a) Yaw angle

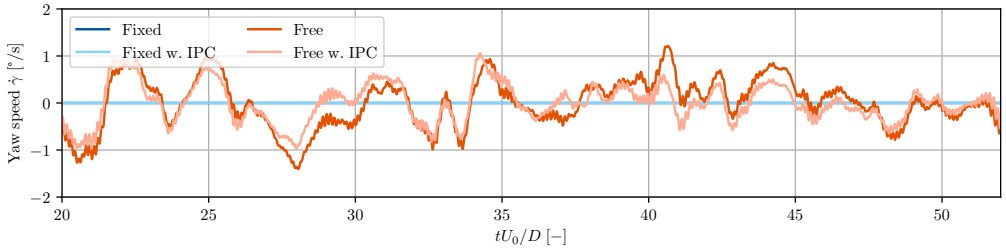

(b) Yaw rate

Figure 4.1: Yaw angle (a) and filtered yaw rate (b) during one Mann's box through-flow for the fixed (blue) and free (orange) cases. Darker and lighter colors stand for the use of the IPC or not, respectively.

but it slightly decreases its mean value. It is because the turbine in free yaw has, in absolute value, an average misalignment angle with the inflow. The turbine is thus less loaded in average. Notwithstanding this lower mean value, the comparison in term of DEL, in Figure 4.4b, shows that the flapwise bending moment is more important in the case of free yaw. It is explained by the fact that the low-frequency oscillations (lower than 1P) are more important in the case of free yaw, as depicted in Figure 4.3 in red. IPC decreases a lot the amplitude of the oscillation and leads to DEL reduction in both cases. Then, from Figure 4.4e one can note that the tangential moment is decreased when the yaw is free and that IPC further decreases it.

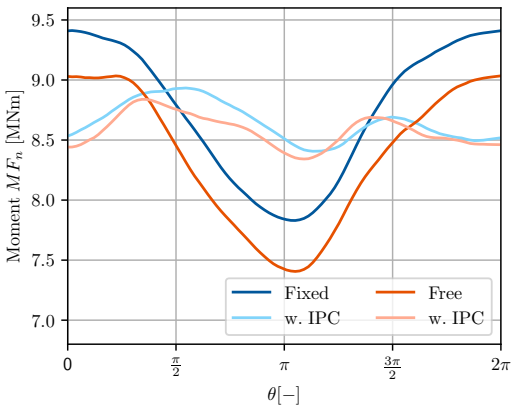

(a) Flapwise bending moment

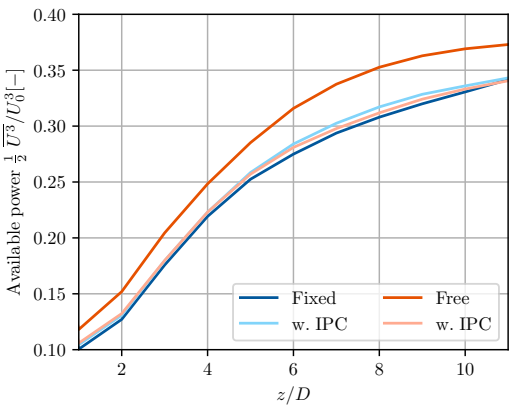

(b) Power downstream

Figure 4.2: Azimuthal evolution of the blades flapwise bending moment (a) for the fixed (blue) and free (orange) cases, without and with IPC. Power in a rotor area behind the wind turbine (b) as a function of the downstream distance from the wind turbine. Darker and lighter colours stand for the use of the IPC or not respectively.

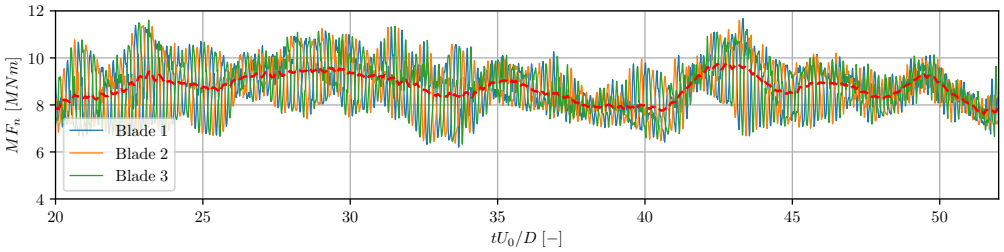

(a) Fixed

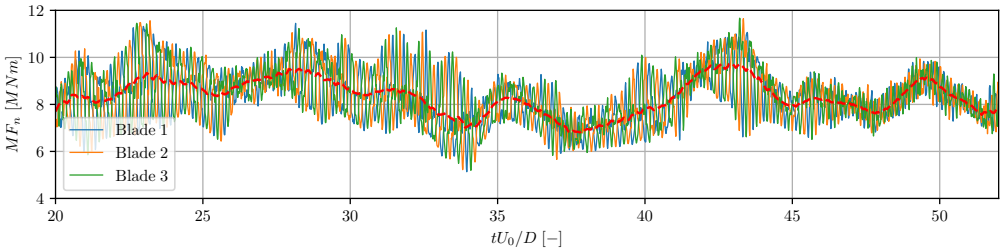

(b) Free

Figure 4.3: Blade flapwise bending moment for both fixed (a) and free (b) yaw cases. The red dashed line represents the low-frequency oscillations, obtained by applying a moving average.

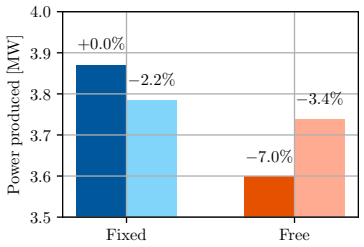

(a) Produced power

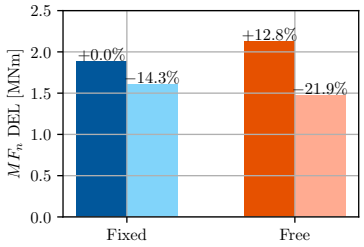

(b) flapwise bending moment

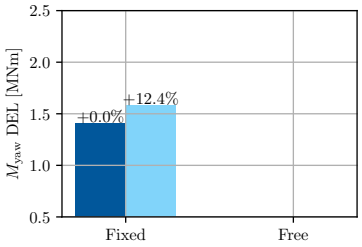

(c) Yaw moment

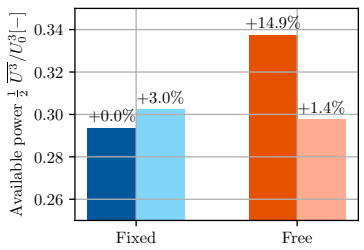

(d) Power downstream

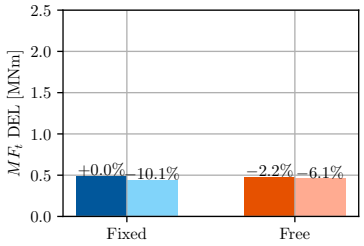

(e) Tangential moment

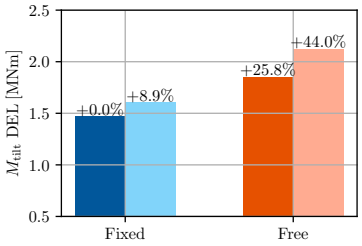

(f) Tilt moment

Figure 4.4: Changes in produced power (a), power available in the wake 7D downstream (d), blade flapwise bending moment damage equivalent loading (b), tangential bending moment damage equivalent loading (e), yaw moment damage equivalent loading (c) and tilt moment damage equivalent loading (f) for the fixed (blue) and free (orange) cases. Darker and lighter colours stand for the use of the IPC or not, respectively. The comparisons are expressed in relative percent compared to the fixed case without IPC.

Contrary to classical wind turbines that have a yaw mechanism to control the yaw angle, a free yawing (downwind) wind turbine does not need it. The cost of the yaw mechanism could thus be saved. Indeed, it stays aligned with the inflow on average even if turbulence makes it oscillate around the inflow direction. When the yaw joint is free, no yaw moment is applied on it. In Figure 4.4c, the yaw moments for the fixed cases are plotted. The effect of IPC is well identifiable. The low-frequency content is well decreased. However, this version of IPC does not reduce the 3P component as it is filtered out from its inputs. It even contributes to increase them and it is the reason for the higher DEL encountered in Figure 4.4 with IPC. The calculations of the DEL takes lower and higher frequencies (3P and higher) into account. Appendix C contains additional comments on IPC and its resultant DEL quantification. Obviously, it is important to notice the correlation between the low-frequency component of the yaw moment, experienced by the fixed turbine, and the evolution of the yaw angle of the free turbine. The yaw moment is translated into yaw motion for the free turbine, with a small lag in time.

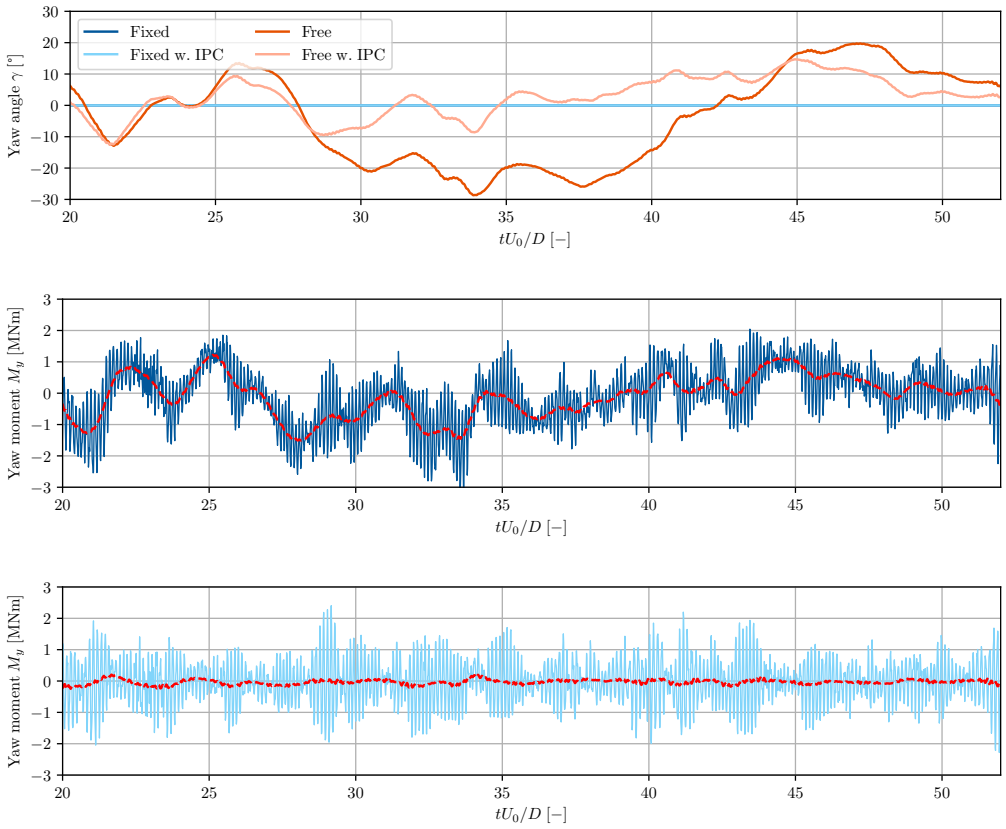

Figure 4.5: Temporal evolution of the yaw angles for the different cases and evolution of the yaw moments for the fixed cases, without and with IPC. Lighter colours denote the use of IPC. The red dashed line is the low-frequency oscillations, obtained by applying a moving average.

The next type of load is the tilt moment. In Figure 4.4f, it is greatly increased by unlocking the yaw motion. From Figure 4.6 where the tilt moment is represented along the time, one can see that it is increased in both low and high-frequency content. On one hand, it might be due to the dynamics of the motion that induces increased aerodynamic solicitations. And on the other hand, it is caused by the gyroscopic moment due to the yaw motion. The gyroscopic moment is given by

$$M_{tilt,gyro} = \dot{\gamma}\, I_{rotor}\, \omega_{rotor}, \tag{4.1}$$

where $\dot{\gamma}$ is the yaw rate, I_{rotor} the inertia of the rotor and ω_{rotor} is the rotating speed of the rotor. For some applications, it can be harmful. For example, for small power turbines, free yaw may require a yaw damping. In fact, they often operate at larger rotational speed and have a larger yaw rate [35]. The induced gyroscopic moment is not that big here. As mentioned earlier, we are in a reasonable range of yaw rates. In Figure 4.6, no drastic increase is noticed. Investigations led in Appendix B.1 show that the wind turbine can largely withstand the gyroscopic moment encountered. Moreover, shear is more harmful. Again, we can note the effect of IPC reducing the low-frequency content. The reduction is more effective in the fixed case than in the free yaw case.

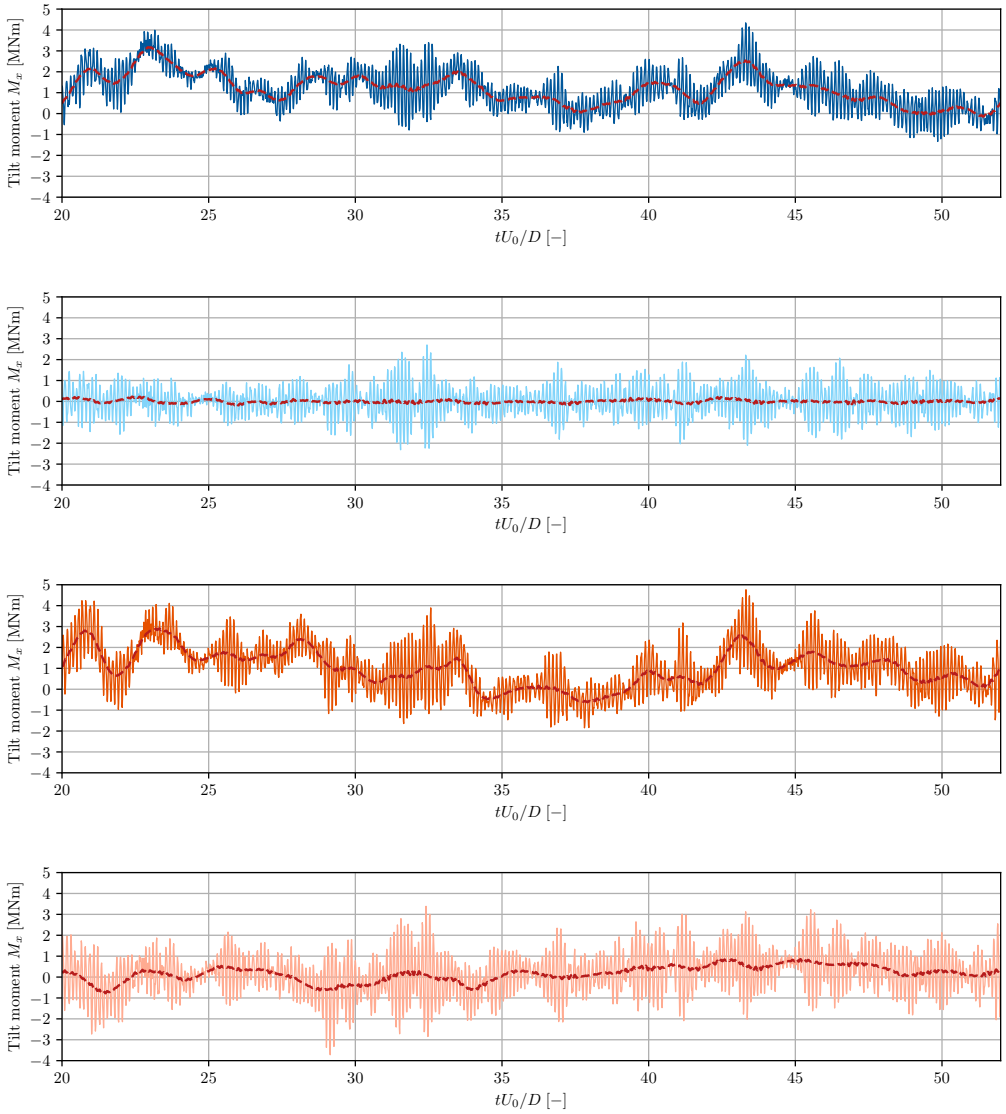

Figure 4.6: Temporal evolution of the tilt moments at the articulation for the fixed (blue) and free (orange) cases. Lighter colours denote the use of IPC. The red dashed line is the low-frequency oscillation, obtained by applying a moving average.

Let us now elaborate on the power. First, the power produced by the free yawing turbine is lower, as shown in Figure 4.4a. One could think that as the turbine self aligns with the inflow it would produce more. Conversely, it produces less because it actually oscillates around the inflow direction due to the large turbulence structures. The turbine gathers less power for the time it spends not aligned with the inflow. Here the effect of IPC is different for the two cases. For

the yaw locked turbine, it tends to decrease the power production as already explained in the previous chapter. For the free yawing case, we saw that the amplitude of the oscillation around the inflow direction is damped by the IPC (Figure 4.1a). The turbine alignment with the inflow is thus better than for the free case without IPC. Hence, IPC leads to a higher power in the free case but still less than both fixed cases.

Regarding the power available downstream, from Figure 4.4d, a significant gain is achieved in free yaw. Further, from Figure 4.3b, the gain in power available downstream grows with the downstream distance from the turbine. Again, IPC reduces the effect of the free yaw and cancels the power gain in the wake. For the fixed yaw case, the effect of IPC is really small and induces a decrease in the available power.

As already explained, the wake behaviour is of capital importance when talking about the power available for a downstream wind turbine in the context of wind farms. To clarify what occurs in the case of free yaw, some investigations are made to better understand what takes place. In Figure 4.7a, the amplitude of the meandering is computed as a function of the downstream position. The free yaw case has a larger amplitude than the other. Also, it is growing faster with the downstream distance. The other cases present similar amplitudes. Regarding the wavelength of the meandering, the free yaw case has a larger wavelength closer to the turbine. The two IPC case are really close and the evolution of the wavelength with the downstream distance is concave and has a maximum around 6D. However, for the fixed case, it is approximately flat.

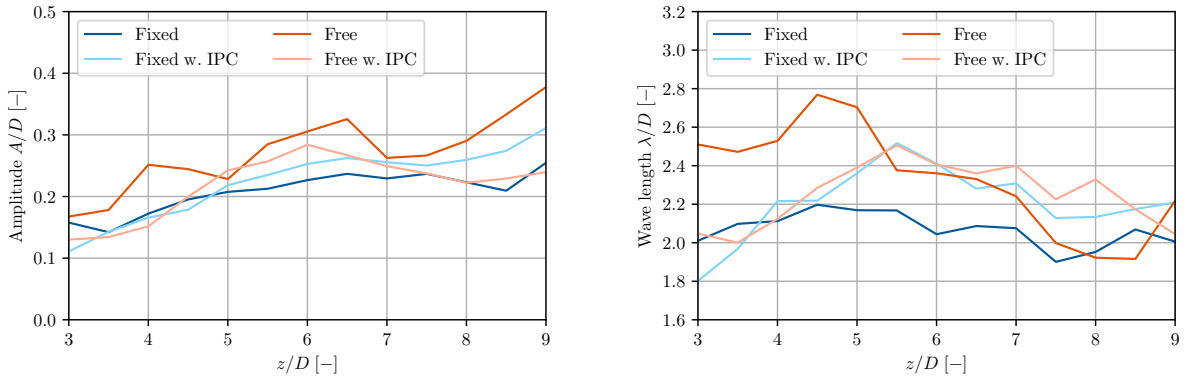

(a) **(b)**

Figure 4.7: Mean binned wake amplitudes (a) and wavelengths (b) with respect to the downstream location for the fixed (blue) and free (orange) cases. Lighter colours denote the use of IPC.

The accentuated meandering provided by the free yaw contributes to increased wake mixing. In Figure 4.8, velocity profiles at different downstream locations are presented. For the fixed case, IPC has nearly no impact on the recovery, as the amplitude are similar for those cases. The faster recovery of the free yaw case is well identifiable. It is the cause of the energy gain pointed earlier, for a downstream the turbine. The velocity deficit is smaller and wider. When IPC is added to free yaw, the velocity deficit is relatively close to the one obtained for two fixed cases. However, the velocity deficit is thinner and slightly shifted toward negative x.

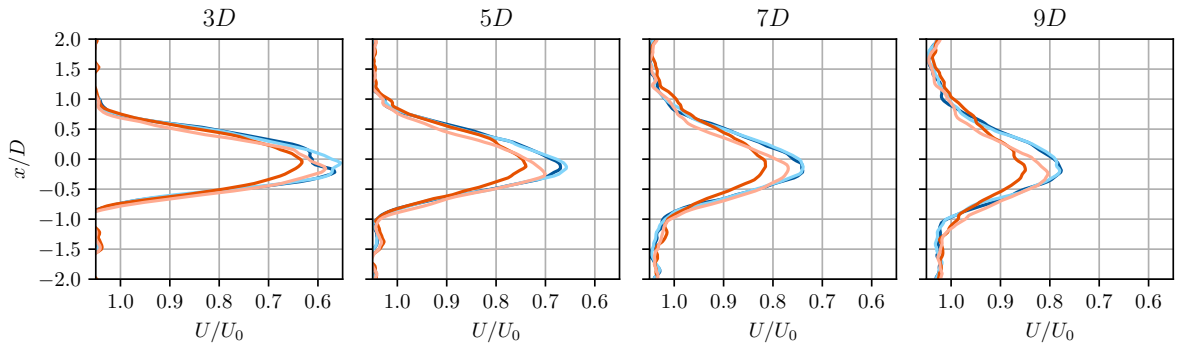

Figure 4.8: Mean velocity profiles for the fixed (blue) and free (orange) cases for several downstream positions. Lighter colours denote the use of IPC.

4.4 Conclusion

At the beginning of the chapter, the goal of the strategy was recalled with the motivations. This strategy is about wake dissipation and is motivated by the quite complex dynamic strategies tested up till now in the literature.

Secondly, the numerical setup was addressed. It is to note that the tower is not modelled here and that a next step would be to include it in a similar study. The wake tracking algorithm was also used to identify the impact of free yaw on the wake.

Then the results were presented. The free yawing turbine is stable and does not experience too high yaw rates. Free yaw accentuates the wake meandering motion that leads to a faster recovery and increases the power available downstream. It also allows getting rid of the yaw mechanism a classical wind turbine needs. However, the other loading types are increased and the turbine power production is decreased. The usage of IPC was showed to cancel what is brought up by free yaw. It reduces the variation of the yaw angle and yaw rate, it cancels the power gain in the wake and mitigates the additional loading induced. The use of IPC seems therefore not indicated in combination with free yaw. Regarding the wake, except the increased meandering, no other impact on the wake were identified.

Free yaw has thus proven its potential to increase the power in the wake by an enhancement of the meandering motion. However, similar or larger increases in meandering were reported for static yaw misalignment in the previous chapter. The power loss it induces is not negligible. In addition, it also causes more fatigue. Like in the previous chapter, it would be interesting to lead a deeper investigation, considering the LCOE to assess its worthiness or not. Nevertheless, it does not seem that interesting considering the advantages and drawbacks pointed out. A deeper study of the wake behaviour with more performant tools could also help to better highlight the impact of free yaw.

Chapter 5

Optimal strategy for a pair of inline wind turbines

In previous chapters, different strategies were presented. Both redirections and dissipations techniques were addressed. This chapter is about simulations where two wind turbines are considered. The first wind turbine is implemented with the best strategy of each previous chapter with their IPC version. Then the different quantities of interest are studied for both wind turbines. Of course, in this chapter, the focus is on the second wind turbine and the impact of the chosen strategies for the upstream wind turbine on it. The effects of those strategies for the turbine that implements it have already been discussed in the previous chapters. The first section presents the numerical setup. Then the results are analysed in the second section. And finally, the chapter is ended with a conclusion.

5.1 Numerical setup

To study the impact of using a certain control, cases with two wind turbines are run. For all the cases studied, only the upstream wind turbine is used with an additional control while the second is used with its regular control. The first case does not feature any particular control and serves as a reference case. In the second case, the upstream wind turbine has a static yaw misalignment of $\gamma = 20°$. For the third case, free yaw is enabled for the first wind turbine. For all those three cases, the addition of IPC on the first turbine is also performed, totalling six different cases. In each case, the impact on the power produced and the loads experienced by the second wind turbine are analysed. Also, the mean power output and solicitations for the two turbines are considered to evaluate the efficiency of the control strategies at the level of the wind turbine pair.

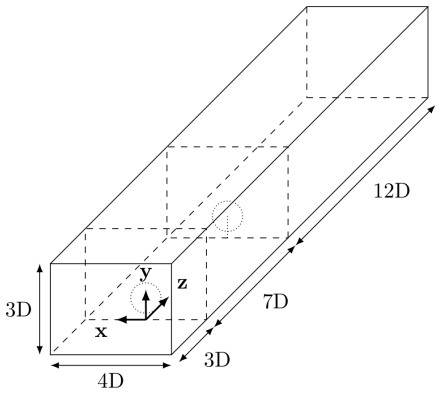

Figure 5.1: Computational domain.

Again, the study is carried out with numerical simulations using the LES code *VPM* and the multibody solver ROBOTRAN. The quantification of the fatigue loading is evaluated with Damage Equivalent Loading and relies on rainflow counting. Similar simulation parameters as for the other chapters are used. The simulations are performed using the NREL-5MW wind turbine. Note that the turbine is considered in upwind configuration, except for the free yaw cases where the turbine is used in downwind configuration. No blade coning nor nacelle tilt are considered and only the blades of the turbines are modelled with immersed lifting lines. The resolution is 32 points per diameter in every direction. The numerical domain is depicted in Figure 5.1. Its width, height and length are $4D \times 3D \times 22D$ and the flow is unbounded in the x and z directions. The first turbine is located at the centre of the domain 3 diameters downstream its entry and the second turbine is 7D behind the first one. The inflow has a streamwise wind speed at hub height $\mathbf{U_0} = 9\,\mathrm{m/s}$. The turbines are thus working in Region 2 at optimal tip-speed ratio. The wind shear coefficient α is 0.2. A turbulent inflow is synthesized with a Mann box [18] that is 32-diameters long. The time step is constant and the CFL number is between 0.12 and 0.46. The flow is studied after it develops for 20 convective times (4/3 of through-flow) and the different quantities are studied during one Mann box through-flow (32 convective times).

5.2 Results

This section addresses the results obtained, focusing on what the second wind turbine experiences. The results for the pair are also analysed. The aim is to try to identify the best pair, considering the impact of the different strategies studied on the downstream wind turbine.

The streamwise velocity fields are plotted in Figure 5.2. For the misaligned turbine, the redirection of the wake is well identifiable and it encounters the downstream wind turbine on the right. One can note that the wake of the downstream wind turbine is also redirected even if it is aligned with the inflow. Then for the free yawing turbine, the wake exhibits a lower velocity deficit. In what follows, the loads are firstly discussed. Then we look at the power production.

We begin by looking at the blades flapwise bending moment. It is the first thing to look at. Indeed, the stresses are first applied to the blades and are then transferred to the other parts of the turbine. The reference case is denoted "aligned" in Figure 5.3. It corresponds to a basic scenario where both turbines are aligned with the inflow. In that case, the mean azimuthal evolution of the flapwise bending moment of the downstream turbine has a lower mean value than the upstream one because it experiences a lower wind speed. Furthermore, the amplitude is about the same for both wind turbines. One can note that the minimum has moved. It is not at $\theta = \pi$ and it is because the wake does not go straight downstream but it has a little deflection as shown in Figure 3.13. Even if the amplitude of the solicitation is the same on average, the fatigue loading is more important for the downstream turbine, as can be observed in Figure 5.4a. It is caused by the meandering motion of the wake that induces more low frequency (less than 1P) fluctuations in the flapwise bending moment. The use of IPC on the upstream turbine induces higher loads. It is due to the fact that IPC decreases the power extraction at the top and increases it at the top, increasing the top/bottom imbalance (Figure 3.12) for the second wind turbine. The static 20° misalignment is the one that induces the larger blades flapwise bending moment. Contrary to the aligned case, the wake is redirected and instead of experiencing it in the middle, the downstream wind turbine experiences it on the right side creating an important left/right solicitations imbalance. Indeed, one can see from Figure 5.3b that the positions of the extrema are around $\theta = \frac{\pi}{2}$ and $\theta = \frac{3\pi}{2}$. Here IPC induces a slight decrease of the loads. For the free yaw case, the second wind turbine also experiences higher loads. The mean value of the azimuthal evolution is larger than for the reference case because the average inflow velocity is

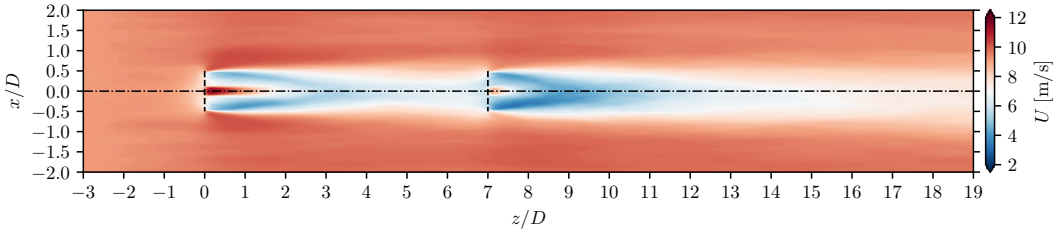

(a) Reference case

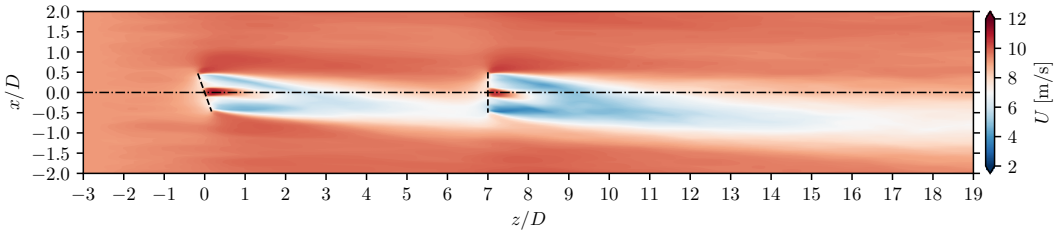

(b) Static yaw misalignment

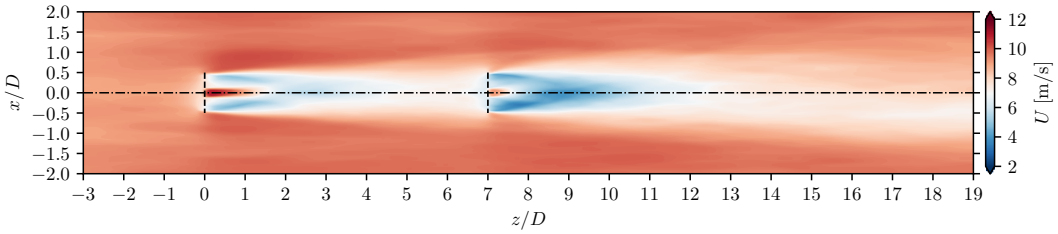

(c) Free yaw

Figure 5.2: Mean streamwise velocity field in a horizontal plane at hub height for two aligned inline wind turbines (a), a 20° misaligned turbine (b) and a free yaw turbine (c) followed with aligned turbines.

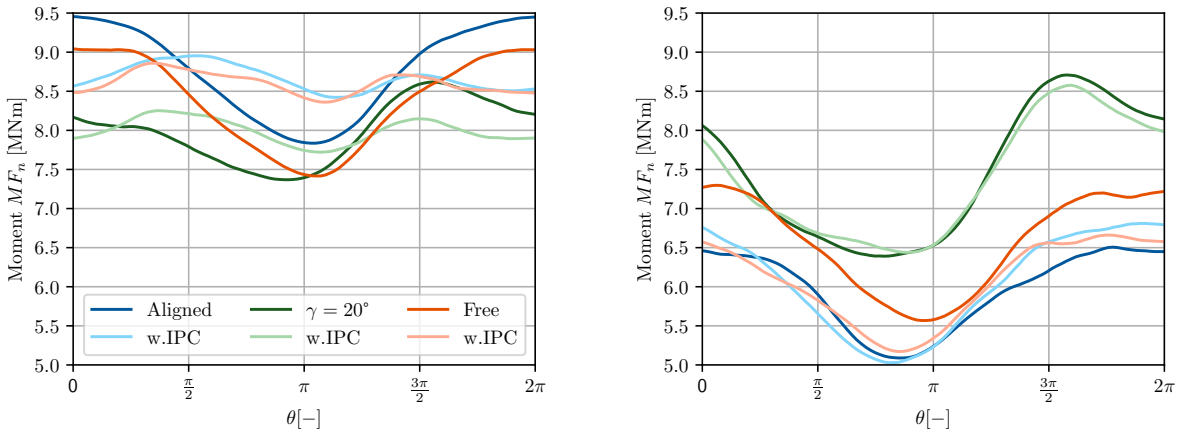

(a) **(b)**

Figure 5.3: Azimuthal evolution of the blades flapwise bending moment of the upstream (a) and downstream (b) wind turbine for the aligned (blue), misaligned (green) and free (orange) cases. Darker and lighter colours stand for the use of the IPC or not, respectively.

higher. Indeed free yaw increases wake mixing and the flow velocity is thus higher. The amplitude is similar compared to the reference case as no additional imbalances are induced by free yaw. The IPC case is really close to the reference case. In fact, we saw in Chapter 4 that IPC tends to kill the effect of free yaw.

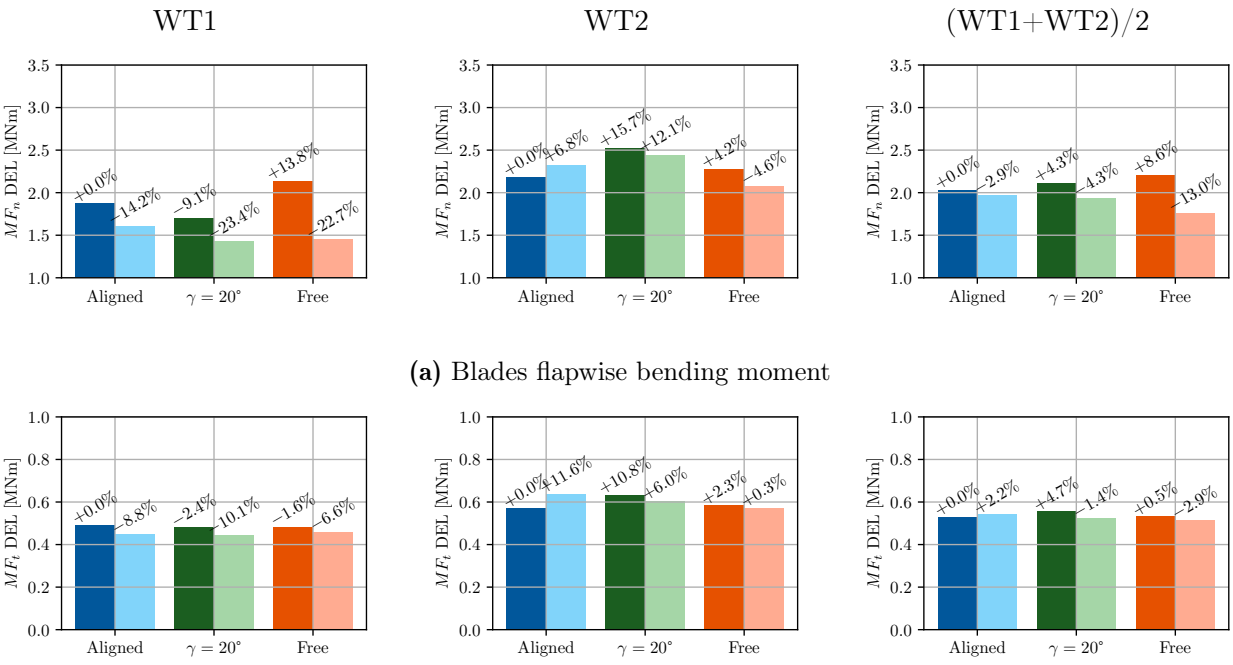

(a) Blades flapwise bending moment

(b) Blades tangential bending moment

Figure 5.4: Changes in blade flapwise bending moment DEL (a) and tangential bending moment DEL (b) for the aligned (blue), misaligned (green) and free (orange) cases. Darker and lighter colours stand for the use of the IPC or not, respectively. The comparisons are expressed in relative percent compared to the aligned without IPC case.

Regarding the tangential bending moment, its DEL quantification is in Figure 5.4b. The tangential bending moment is globally higher for the downstream wind turbine due to the increased turbulence after the first turbine. For the reference case, the loading is more important when using IPC and might be due to the additional imbalances it induces. For the static 20° misalignment, the loading is also increased compared to the reference case. However, the use of IPC on the upstream wind turbine reduces the loading. For the free yaw case, only a slight increase is induced and IPC nearly totally mitigates it.

Let us now focus on the yaw moment, the comparison being depicted in Figure 5.5a. In the reference case, the use of IPC increases the yaw moment. From the blades flapwise bending moment, it is due to the larger imbalance between positions $\theta = \frac{\pi}{2}$ and $\theta = \frac{\pi}{2}$. For the static misalignment case, the loads on the second wind turbine are increased. It directly results from the induced left/right imbalance that induces a more important yaw moment. The uses of IPC on the first turbine further increases the yaw moment on the downstream turbine. An explanation could be the higher velocity bubble, mentioned in Chapter 3, that could further contribute to the left/right imbalance. Free yaw on the upstream wind turbine leads to a slightly higher yaw moment but the use of IPC reduces it.

The tilt moment is increased using IPC on the upstream turbine in the reference scenario. It is due to the higher top/bottom imbalance we just mentioned. In case of static yaw misalignment,

the tilt moment is subject to an increase and IPC again leads to an increase but the effect is small. In the case of free yaw on the upstream wind turbine, the tilt moment is decreased. But the use of IPC, in this case, contributes to a large increase in tilt moment.

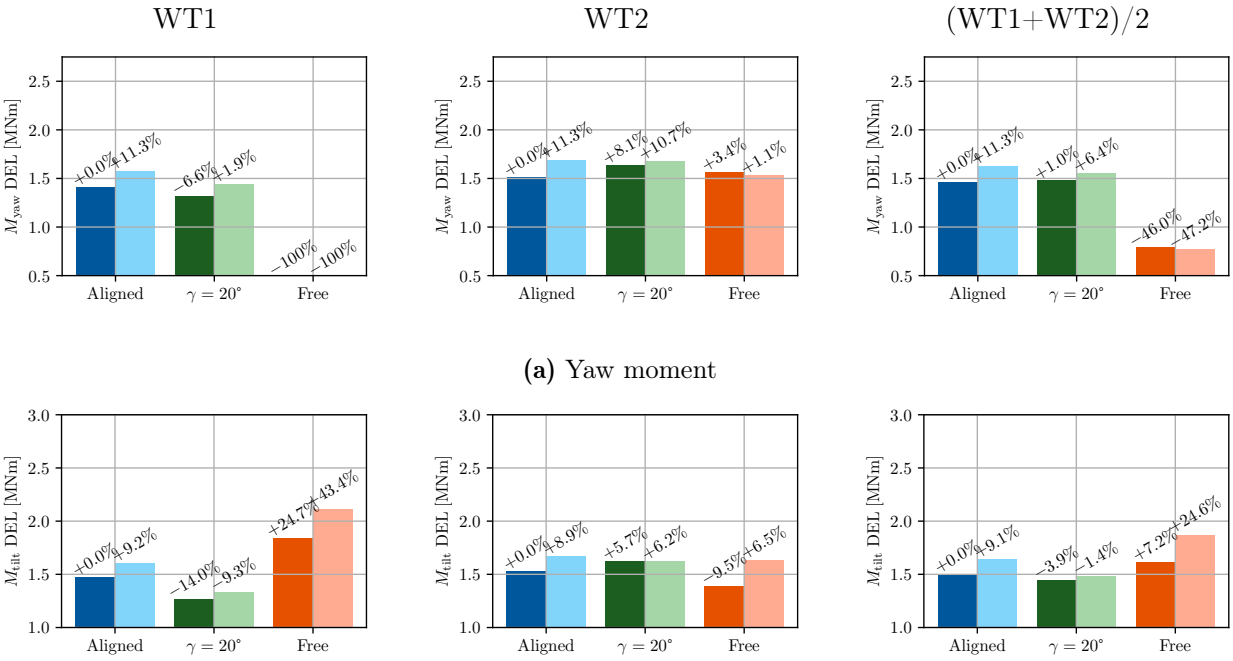

(a) Yaw moment

(b) Tilt moment

Figure 5.5: Changes in yaw moment damage equivalent loading (a) and tilt moment damage equivalent loading (b) for the aligned (blue), misaligned (green) and free (orange) cases. Darker and lighter colours stand for the use of the IPC or not, respectively. The comparisons are expressed in relative percent compared to the aligned without IPC case.

At the level of the wind turbines pair, the use of IPC does not lead to significant differences in terms of blade loads for the reference scenario. But yaw and tilt moment are increased by IPC. When a static misalignment is introduced, the loads are higher for both flapwise and tangential moment but is lower for yaw and tilt moment. It is to be noted that in the frame of upwind wind turbines, the blade flapwise moment is quite important as it has to deal with the tower clearance constraint for the blades not to collide with the tower. The use of IPC, in this case, leads to important blade loads reductions. When the first turbine is in free yaw, the flapwise bending moment is increased a lot, on average for the two turbines. However, it is less critical for downwind wind turbines. The economy of the yaw mechanism is a nice advantage. Nevertheless, there are more solicitations due to the tilt moment. The use of IPC decreases the loads except for the tilt moment.

The power produced by the second turbine is much lower than the power produced by the first one. It is represented in Figure 5.6. The use of IPC in the reference case slightly decreases and increases the power of upstream and downstream turbine respectively. It only results in a slight power loss in the end, when considering both turbines. The static misalignment causes a large power loss at the first turbine but also allows large gains at the second. It leads to a global gain of 4% and IPC only slightly decreases this gain. For the free yaw case, the first wind turbine experiences a power loss and gains are observable at the second. However, it does not result in a significant difference compared to the reference case when both turbines are considered.

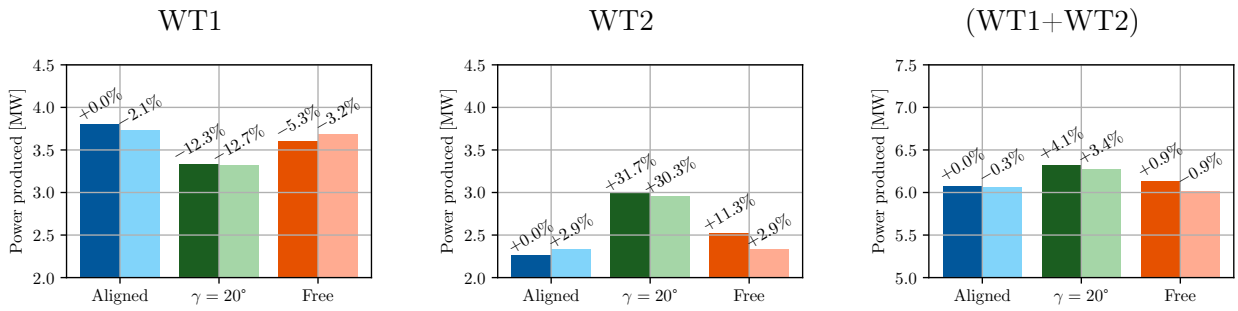

Figure 5.6: Changes in produced power for the aligned (blue), misaligned (green) and free (orange) cases. Darker and lighter colours stand for the use of the IPC or not, respectively. The comparisons are expressed in relative percent compared to the aligned without IPC case.

5.3 Conclusion

In this chapter, the best identified strategies were compared for two inline wind turbines. The impact for the second wind turbine of the different strategies in term of loads was addressed and the power production was also tackled.

The use of IPC without any additional control is poor in term of benefits. The first turbine suffers little and produces much while the second suffers a lot and does not produce much. Here it brings too high loads increases on the second wind turbine compared to the gains on the first one. It does not seem interesting, especially since it does not lead to an increase in power production at the pair level.
As expected, static yaw redirection is really promising. This strategy only leads to slight loads increases and allows a power gain in the end. In this case, the power production is more shared between both turbines. But in term of loads, the uneven repartition is aggravated. Here the combination with IPC helps to mitigate blade loads and tilt moment. It is to be considered as blades loads are more critical. The power loss due to the introduction of IPC is only small.
The case of free yaw is not simple. Used without IPC it increases all the types of loads. However, it could allow the economy of a yaw mechanism. Used with IPC, blade loads are significantly reduced but it adds much tilt moment. In both cases, the gain or loss in power is not significant. Therefore this strategy is not interesting in term of power gain nor loads reduction, except for the IPC case.

As in the other chapters, a deeper study that considers the economic aspects could be led. Nevertheless, it is clear that static yaw misalignment is a strategy that gives an interesting power gain and if combined with IPC also leads to lower loads. On the contrary, free yaw does not provide significant power gains.

Chapter 6

Conclusions and perspectives

With the growing number of wind turbines, the interest on how to optimize the power production at the wind farm level is rising. In this Master's Thesis, we have evaluated power optimization strategies based on yaw, and the effect of combining them with load reducing IPC.

Chapter 1 has been dedicated to presenting the objectives of this Thesis and the context of wind farm control strategies. The goal is to study different strategies that rely on yaw dynamics and analyse their impact on the loads and wake of the wind turbine. For all the studied scenarios, we have addressed the impact of using load reducing IPC. The first strategies under scrutiny have been (1) static yaw misalignment with respect to the inflow direction, (2) simple passive dynamic yaw strategy, and (3) some cases for two inline wind turbines in order to analyse the impact on a downstream wind turbine.

In Chapter 2, we swept through the different tools we have used in this work. Firstly, the flow solver *VPM* has been presented: it combines the advantages of the vortex methods and meshed based approaches. Secondly, the multibody system solver ROBORAN has been discussed: it is based on the generation of symbolic equations and is used to solve the dynamics of the multibody system representing the wind turbine. It is also particularly useful to implement its controllers. Then, we have described the coupling between both numerical solvers: it is done through weak coupling. Both codes run simultaneously and communicate together during synchronization steps, allowing a high modularity. Finally, we have addressed the wind turbine model, including its different controllers. The basic controller of the wind turbine is described, it is based on a generator-torque controller to maximize the power in below-rated operation and a blade-pitch controller to regulate the generator speed in above-rated operation. The second controller is an IPC algorithm based on the Coleman transformation. It aims to mitigate the turbine structural loading due to the variations in the inflow velocity across the wind turbine swept area.

In Chapter 3, we have described the static yaw misalignment strategy, and examined what happens in two steps: without turbulences, then with turbulences. Static yaw misalignment is a well-known strategy, but its combination with IPC is less covered. In the methodology we have presented a low complexity wake tracking algorithm relying on a 3D convolution of the power in a horizontal plane. Then we have examined what happens. First, we have investigated turbulence-less cases to introduce and illustrate the basic loads and wake physics when using static yaw misalignment. Positively oriented yaw misalignment counters the imbalance caused by the shear in the inflow, while negative yaw tends to increase imbalances. Another point is the high and low-velocity zones induced in the wake by IPC. The direction of the wake redirection matters. Depending on the redirection, a downstream wind turbine can potentially either encounter the higher or lower velocity zone; with positive yaw, an inline downstream wind turbine will experience the higher velocity zone. Secondly, we have analysed the turbulent cases. This analysis gives more reliable quantifications of loads and power. For every type of load, we have seen that

the fatigue loading is more important for negative yaw. The use of IPC showed a great potential at reducing blades loads. However, the current version of IPC increases the yaw and tilt moment. Regarding the power, positive yaw is again better as the power production and the power available downstream are larger. The tendency of the wake to have increasing meandering with misalignment has been identified. We also have found that the increase in meandering is larger for negative yaw angles. The velocity deficit is thus smaller but also wider than for positive yaw. The conclusion of this chapter is that positive yaw appears to be the most promising redirection strategy, and that the load reduction IPC provides is worth the small power loss it induces.

Chapter 4 addressed free yaw as a simple passive dynamic yaw strategy. To date, only complex dynamic yaw strategies have been studied in the literature for large wind turbines. In our study, we have shown that the turbine remains stable and that the yaw rate stays in a reasonable range. Free yaw induces increased fatigue loadings on the turbine. The fact that the turbine rotates along its yaw axis also induces an additional tilt moment due to gyroscopic effects, but it was not critical in our investigations. The use of IPC in combination with free yaw mitigates the extra loads except for the tilt moment. Free yaw does not require a yaw mechanism and it can show an economical advantage. In addition, even if it reduces the power output, free yaw has a great potential at increasing the amplitude of the wake meandering. It allows for a faster wake recovery and important gains in power downstream. On the contrary, the use of IPC cancels the meandering brought by free yaw. Free yaw combined with IPC then exhibits similar wake characteristics as the normal case. The advantage of using free yaw is not straightforward. The increased loads are not worth the power gains in the wake. Indeed, similar increases in meandering are achieved with static misalignment. Moreover, larger power gains downstream can be obtained with static yaw misalignment.

In Chapter 5, we have investigated small wind farms of two inline wind turbines. The first turbines are featured with the control strategies that showed to be the best in the previous chapter. For each case, loads and power output have been considered for both turbines. The misaligned turbine scenario leads the comparison and yields the highest power output at wind farm level. Its combination with IPC seems the best compromise as the additional loads caused by the misalignment are mitigated. Also, the total amount of loads at the pair level is lower than for the reference case. Free yaw does not allow interesting power gains compared to the high induced structural loading. Its combination with IPC is not worth it.

In summary, positive static yaw misalignment is an excellent strategy to increase the power for a downstream wind turbine. The addition of IPC allows for relevant loads reduction. Based on the investigations performed in this study, the advantages of free yaw are still to prove. Besides, structural load considerations would benefit from deeper analysis to identify the most harmful loading modes, in order to support our conclusions. In the different chapters, we have also mentioned the possibility of using Levelised Cost of Energy (LCOE) and a Life Cycle Assessment (LCA) to have more meaningful quantifications of the efficiency of the different strategies. Regarding the wake behaviour, we have only used a low complexity tool to underline some wake characteristics but the use of more performant tools should also be considered. In addition, the efficiency of the IPC algorithm we use may depend on the inflow velocity and turbulence intensity. The gains of its PI controller could still be improved by reviewing and optimizing its response in a wider range of scenarios.

Bibliography

[1] European Commission. *The European Green Deal*. Number COM(2019) 640. Brussels, 12 2019.

[2] European Commission. *An EU Strategy to harness the potential of offshore renewable energy for a climate neutral future*. Number COM(2020) 741. Brussels, 11 2020.

[3] S. Boersma, B.M. Doekemeijer, P.M.O. Gebraad, P.A. Fleming, J. Annoni, A.K. Scholbrock, J.A. Frederik, and J-W. van Wingerden. A tutorial on control-oriented modelling and control of wind farms. In *American Control Conference (ACC)*, pages 1–18, 2017.

[4] W. Munters and J. Meyers. Dynamic strategies for yaw and induction control of wind farms based on Large-Eddy Simulation and optimization. *Energies*, 11(1):177, January 2018.

[5] J. A. Frederik, R. Weber, S. Cacciola, F. Campagnolo, A. Croce, C. Bottasso, and J.-W. van Wingerden. Periodic dynamic induction control of wind farms: proving the potential in simulations and wind tunnel experiments. *Wind Energy Science*, 5(1):245–257, 2020.

[6] P. Fleming, P. M.O. Gebraad, S. Lee, J-W. van Wingerden, K. Johnson, M. Churchfield, J. Michalakes, P. Spalart, and P. Moriarty. Evaluating techniques for redirecting turbine wakes using SOWFA. *Renewable Energy*, 70:211 – 218, 2014. Special issue on aerodynamics of offshore wind energy systems and wakes.

[7] M. Howland, S. Lele, and J. Dabiri. Wind farm power optimization through wake steering. *Proceedings of the National Academy of Sciences*, 116(29):14495–14500, 2019.

[8] J. Frederik, B. Doekemeijer, S. Mulders, and J-W. van Wingerden. On wind farm wake mixing strategies using dynamic individual pitch control. *Journal of Physics: Conference Series*, 1618:022050, sep 2020.

[9] E. A. Bossanyi. Individual blade pitch control for load reduction. *Wind Energy*, 6(2):119–128, 2003.

[10] C. Wang, F. Campagnolo, and C. L. Bottasso. Does the use of load-reducing IPC on a wake-steering turbine affect wake behavior? *Journal of Physics: Conference Series*, 1618:022035, 9 2020.

[11] P. Chatelain, S. Backaert, G. Winckelmans, and S. Kern. Large Eddy Simulation of wind turbine wakes. *Flow, Turbulence and Combustion*, 91, 10 2013.

[12] P. Chatelain, A. Curioni, M. Bergdorf, D. Rossinelli, W. Andreoni, and P. Koumoutsakos. Billion vortex particle direct numerical simulations of aircraft wakes. *Computer Methods in Applied Mechanics and Engineering*, 197(13):1296–1304, 2008.

[13] S. Backaert, P. Chatelain, and G. Winckelmans. Vortex particle-mesh with immersed lifting lines for aerospace and wind engineering. *Procedia IUTAM*, 18:1–7, 2015. IUTAM Symposium on Particle Methods in Fluid Dynamics.

[14] G. Winckelmans. *Vortex Methods*, pages 1–24. American Cancer Society, 2017.

[15] P. Chatelain and P. Koumoutsakos. A Fourier-based elliptic solver for vortical flows with periodic and unbounded directions. *Journal of Computational Physics*, 229(7):2425–2431, 2010.

[16] H. Jeanmart and G. Winckelmans. Investigation of eddy-viscosity models modified using discrete filters: A simplified "regularized variational multiscale model" and an "enhanced field model". *Physics of Fluids*, 19(5):055110, 2007.

[17] J.D. Anderson. *Fundamentals of Aerodynamics*. College Ie Overruns. McGraw-Hill Education, 2016.

[18] J. Mann. The spatial structure of neutral atmospheric surface-layer turbulence. *Journal of Fluid Mechanics*, 273:141–168, 1994.

[19] P. Fisette and Q. Dociquer. Modelling Multibody Systems with ROBOTRAN. 2020.

[20] N. Docquier, A. Poncelet, and P. Fisette. ROBOTRAN: a powerful symbolic generator of multibody models. *Mechanical Sciences*, 4(1):199–219, 2013.

[21] S. Buffin. Simulation of rotorcraft dynamics through the coupling of a multibody solver and a vortex particle-mesh method. Master's thesis, University of Louvain-la-Neuve, 2016.

[22] J. Jonkman, S. Butterfield, W. Musial, and G. Scott. Definition of a 5MW reference wind turbine for offshore system development. *National Renewable Energy Laboratory (NREL)*, 02 2009.

[23] A. Jiménez, A. Crespo, and E. Migoya. Application of a LES technique to characterize the wake deflection of a wind turbine in yaw. *Wind Energy*, 13(6):559–572, 2010.

[24] E. A. Bossanyi. Further load reductions with individual pitch control. *Wind Energy*, 8(4):481–485, 2005.

[25] S. Kanev and T.G. Engelen. Exploring the limits in individual pitch control. *European Wind Energy Conference*, pages 1–10, 03 2009.

[26] G. Freebury and W. Musial. Determining equivalent damage loading for full-scale wind turbine blade fatigue tests. *National Renewable Energy Laboratory (NREL)*, 3 2000.

[27] Standard practices for cycle counting in fatigue analysis. Standard ASTM E1049-85, ASTM International, West Conshohocken, PA, 2017.

[28] N. Coudou. *Numerical and experimental investigations of the meandering phenomenon in wind turbine wakes*. PhD thesis, University of Louvain-la-Neuve, University of Mons, von Karman Institute for Fluid Dynamics, 2 2021.

[29] D. R. S. Verelst, T. J. Larsen, and J-W. van Wingerden. Wind tunnel tests of a free yawing downwind wind turbine. *Journal of Physics: Conference Series*, 555:012103, dec 2014.

[30] C. Kress, N. Chokani, and R.S. Abhari. Downwind wind turbine yaw stability and performance. *Renewable Energy*, 83:1157–1165, 2015.

[31] Q. Zhao, C. Sheng, and A. Afjeh. Computational aerodynamic analysis of offshore upwind and downwind turbines. *Journal of Aerodynamics*, 10 2014.

[32] B. Dose, H. Rahimi, B. Stoevesandt, and J. Peinke. Fluid-structure coupled investigations of the NREL 5 MW wind turbine for two downwind configurations. *Renewable Energy*, 146:1113–1123, 2020.

[33] M. Reiso. *The Tower Shadow Effect in Downwind Wind Turbines*. PhD thesis, Norwegian University of Science and Technology, 02 2013.

[34] X. Wang, Z. Ye, S. Kang, and H. Hu. Investigations on the unsteady aerodynamic characteristics of a horizontal-axis wind turbine during dynamic yaw processes. *Energies*, 12(16), 2019.

[35] J. Tangler. Advanced wind turbine design studies - advanced conceptual study - final report. Technical Report NREL/TP-442-4740, NREL - National Renewable Energy Laboratory, United States, 8 1994.

Appendix A

Static misalignment

A.1 Sheared inflow

	Power		**MF_n DEL**		**Available power in the wake 7D downstream**	
IPC	Off	On	Off	On	Off	On
−30°	-25.8%	-29.1%	+26.8%	-63.6%	+154.0%	+127.4%
−20°	-11.3%	-15.5%	+20.6%	-63.3%	+110.8%	+100.2%
−10°	-2.8%	-6.7%	+10.5%	-73.7%	+26.4%	+33.1%
0°	0	-3.1%	0%	-83.1%	0%	-5.7%
10°	-2.9%	-4.9%	-21.1%	-78.2%	+35.5%	+38.0%
20°	-11.8%	-12.3%	-31.9%	-73.4%	+100.4%	+101.2%
30°	-25.7%	-25.5%	-42.7%	-63.5%	+134.1%	+133.9%

Table A.1: Changes in produced power, blade flapwise bending moment damage equivalent loading (DEL) and power in wake for the different yaw angles, with and without IPC. The comparisons are expressed in relative percent compared to the 0° without IPC case.

A.2 Turbulent sheared inflow

	Power		**Available power in the wake 7D downstream**	
IPC	Off	On	Off	On
−30°	-27.1%	-29.8%	+41.6%	+40.0%
−20°	-12.4%	-15.4%	+25.3%	+24.4%
−10°	-3.2%	-6.0%	+5.0%	+5.3%
0°	0%	-2.2%	0%	+3.0%
10°	-2.9%	-4.3%	+12.8%	+13.4%
20°	-12.1%	-12.5%	+36.4%	+35.9%
30°	-26.6%	-26.5%	+48.9%	+48.9%

Table A.2: Changes in produced power and power in the wake for the different yaw angles, with and without IPC. The comparisons are expressed in relative percent compared to the 0° without IPC case.

	$\mathbf{MF_n}$ **DEL**		$\mathbf{MF_t}$ **DEL**		$\mathbf{M_{yaw}}$ **DEL**		$\mathbf{M_{tilt}}$ **DEL**	
IPC	Off	On	Off	On	Off	On	Off	On
−30°	+2.4%	-24.8%	-18.7%	-24.8%	-8.6%	+1.0%	-22.6%%	-17.2%
−20°	+6.9%	-17.6%	-10.7%	-15.8%	-2.1%	+9.4%	-9.4%%	-1.0%
−10°	+4.9%	-13.6%	-3.8%	-12.2%	+0.7%	+12.0%	-1.1%	+8.3%
0°	0%	-14.3%	0%	-10.1%	0%	+12.4%	0.0%	+8.9%
10°	-5.0%	-19.0%	+0.7%	-5.0%	-2.1%	+9.1%	-4.4%	+3.0%
20°	-9.5%	-23.9%	-3.2%	-9.5%	-6.4%	+2.3%	-14.2%	-9.0%
30°	-16.4%	-30.4%	-11.5%	-16.6%	-11.7%	-6.0%	-27.0%	-25.1

Table A.3: Changes in the damage equivalent loading (DEL) of different bending moments: blade flapwise bending moment, tangential bending moment (drivetrain), yaw moment (yaw bearing) and tilt moment (tower); for the different yaw angles, with and without IPC. The comparisons are expressed in relative percent compared to the 0° without IPC case.

	6D		**7D**		**8D**	
IPC	Off	On	Off	On	Off	On
−30°	0.30	0.29	0.32	0.30	0.36	0.35
−20°	0.32	0.26	0.32	0.26	0.34	0.26
−10°	0.11	0.12	0.11	0.12	0.11	0.13
0°	-0.06	-0.09	-0.09	-0.10	-0.12	-0.14
10°	-0.26	-0.23	-0.30	-0.27	-0.32	-0.30
20°	-0.42	-0.42	-0.43	-0.47	-0.51	-0.52
30°	-0.45	-0.47	-0.51	-0.51	-0.55	-0.55

Table A.4: Mean wake centerline position for the different cases at 6, 7 and 8D downstream, normalized with the diameter.

	6D		**7D**		**8D**	
IPC	Off	On	Off	On	Off	On
−30°	0.35	0.35	0.38	0.38	0.37	0.39
−20°	0.19	0.20	0.24	0.26	0.27	0.29
−10°	0.18	0.15	0.19	0.15	0.22	0.19
0°	0.16	0.16	0.17	0.18	0.19	0.22
10°	0.13	0.15	0.15	0.15	0.18	0.18
20°	0.14	0.16	0.21	0.23	0.24	0.22
30°	0.24	0.25	0.26	0.28	0.28	0.32

Table A.5: Standard deviation of the wake centerline position for the different cases at 6, 7 and 8D downstream, normalized with the diameter.

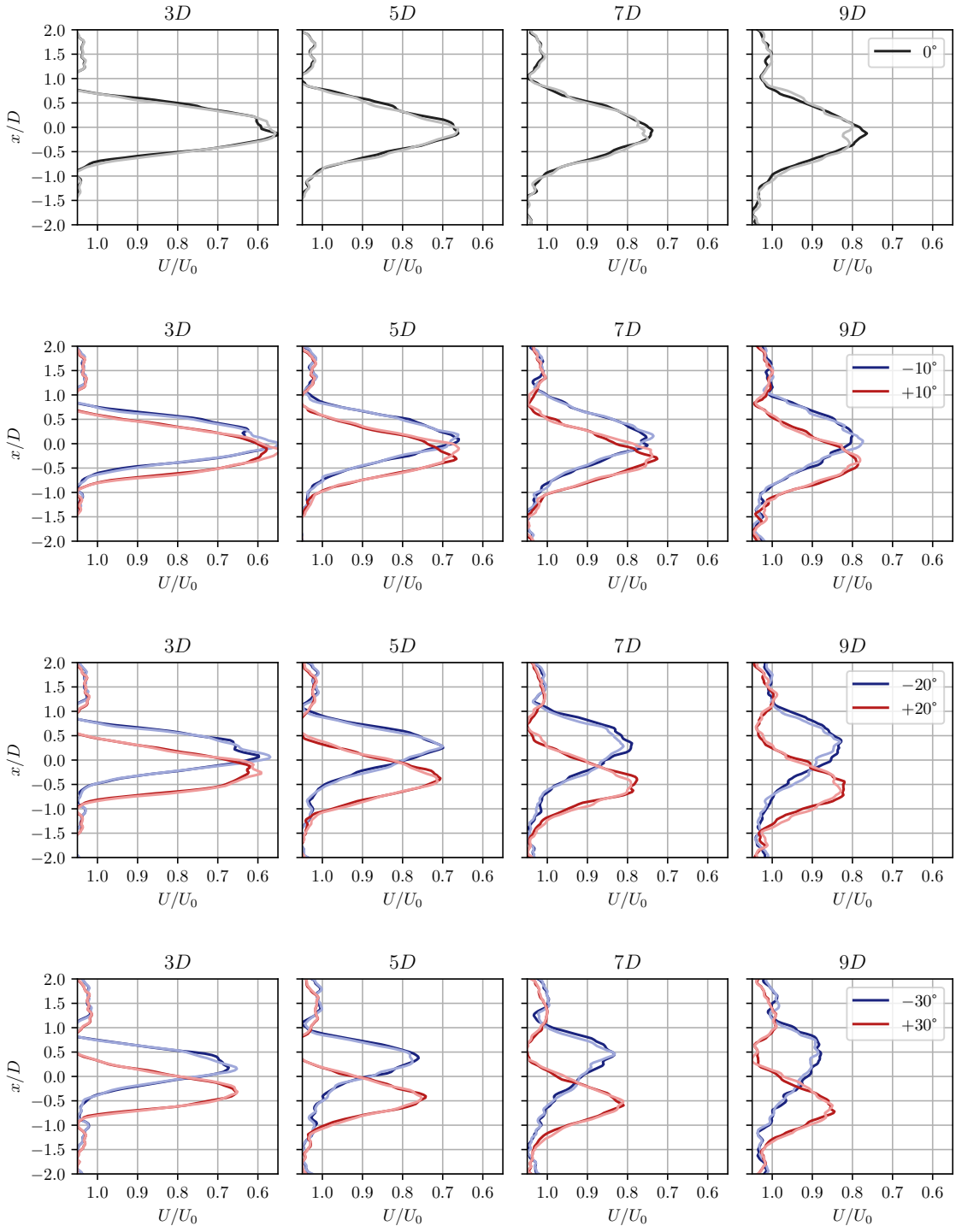

Figure A.1: Mean velocity profile for the different cases for several downstream positions. Darker and lighter stands for non-IPC and IPC cases respectively.

Appendix B

Dynamic yaw misalignment

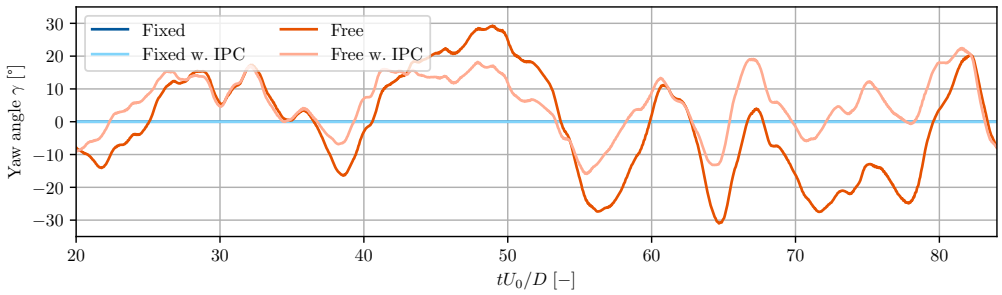

(a) Yaw angle

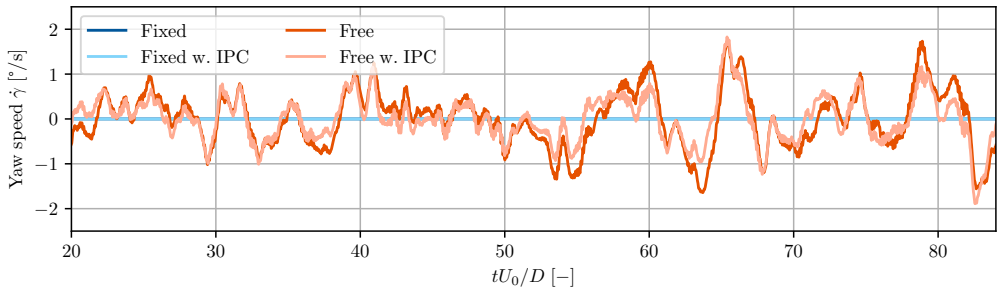

(b) Yaw rate

Figure B.1: Yaw angle (a) and filtered yaw rate (b) during one Mann's box flow through for the cases, with and without IPC. A Mann's box of 64D is used.

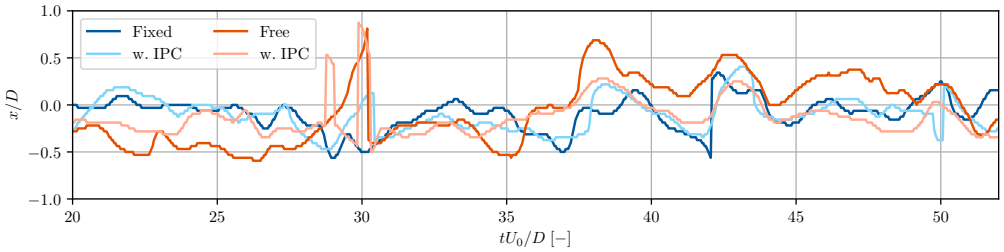

Figure B.2: Transverse wake position at 7D downstream for the different cases.

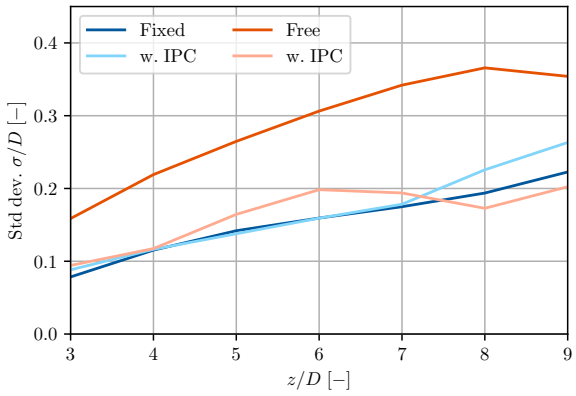

Figure B.3: Standard deviation of the transverse wake position as a function of the downstream distance from the turbine for the different cases.

B.1 Gyroscopic moment

This appendix presents a few investigations regarding the gyroscopic moment induced by the yaw motion. The main goal is to have an idea of the tilt moment the turbine can withstand and compare it to the gyroscopic moment encountered in chapter 4. Just note that the data from turbulent simulations displayed in this appendix are run with a 24-diameter Mann box.

The first thing tested here is the accuracy of

$$M_{\text{tilt,fixed}} \stackrel{?}{=} M_{\text{tilt,free}} - M_{\text{gyro}}. \tag{B.1}$$

It is displayed in Figure B.4b. One can see that it is only true when the misalignment angle is small, like around 33 and 42 convective times. The difference grows as the misalignment increase and is due to aerodynamic effects.

In Figure B.5, a test is done by imposing the yaw displacement and the yaw speed. The yaw speed is 0.3 °/s rms, which correspond to the rated speed of the actuator and the yaw angle oscillates between −30° and 30°. The goal is to evaluate the relative importance of the gyroscopic moment and have an idea of the tilt moment the turbine could encounter in normal conditions. To do so, we have one case at 9 m/s like for our other simulation and another at 15 m/s. Those simulations have been run with shear but without turbulence to better see the effect of the gyroscopic moment. All the other parameters are similar to the other simulation ran in chapter 4. First from Figure B.5d, at 9 m/s, one can see the impact of the gyroscopic around 35 convective times. For the rest, the tilt moment is influenced by the yaw angle and thus by the effect of the shear. At 15 m/s, in Figure B.5f the gyroscopic effect is nearly not visible anymore and the tilt moment is driven by the shear. Already, tilt moment values are in the range of those obtained for the free yaw case (Figure B.5b). As the turbine operates until 25 m/s, we expect it could withstand an even higher tilt moment, from the shear, than what is encountered for our free yaw study. (The gyroscopic moment is only represented for 9 m/s in Figure B.5 because it is only slightly lower for 15 m/s. It is proportional to the rotation speed that decreases with the inflow velocity speed.)

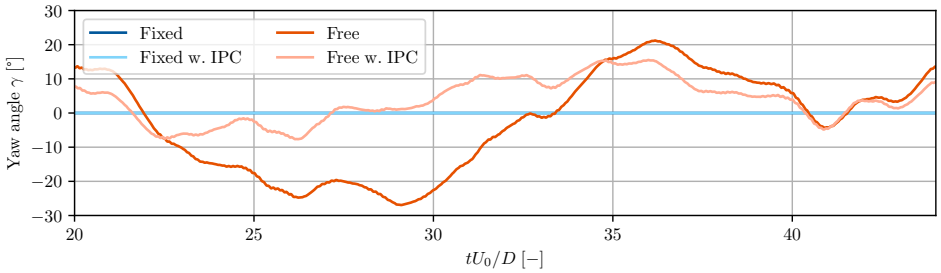

(a)

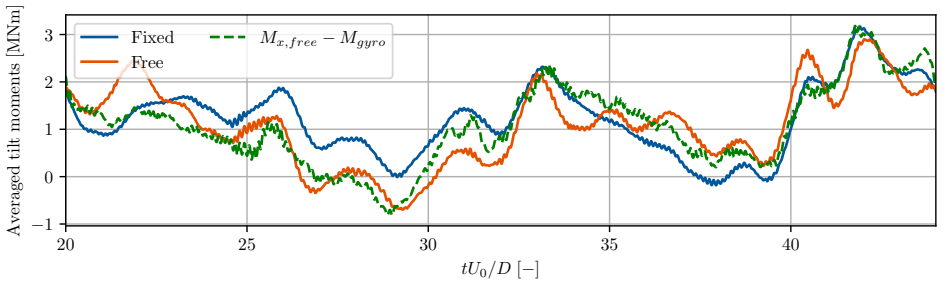

(b)

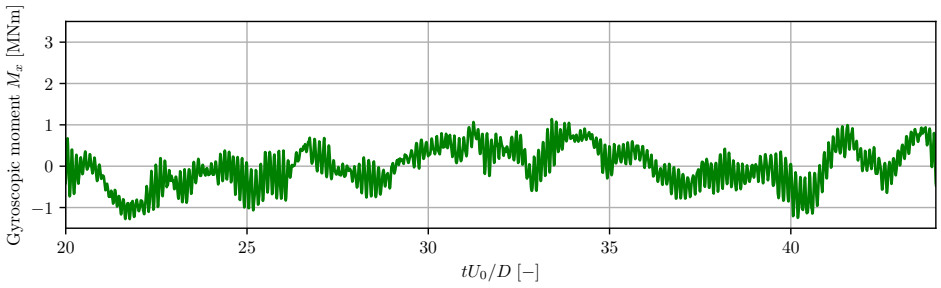

(c)

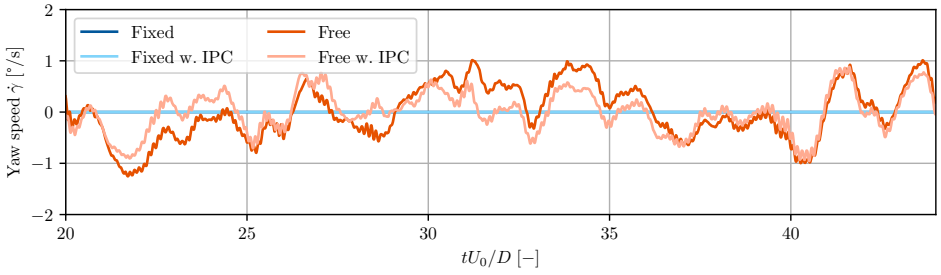

(d)

Figure B.4: Evolution of the yaw angle (a). Filtered tilt moments at the articulation for the fixed and free cases without IPC (b). In red is the filtered tilt moment of the free yaw case subtracted with the gyroscopic moment. Gyroscopic moment of the free yaw case without IPC (c). Yaw rates (d).

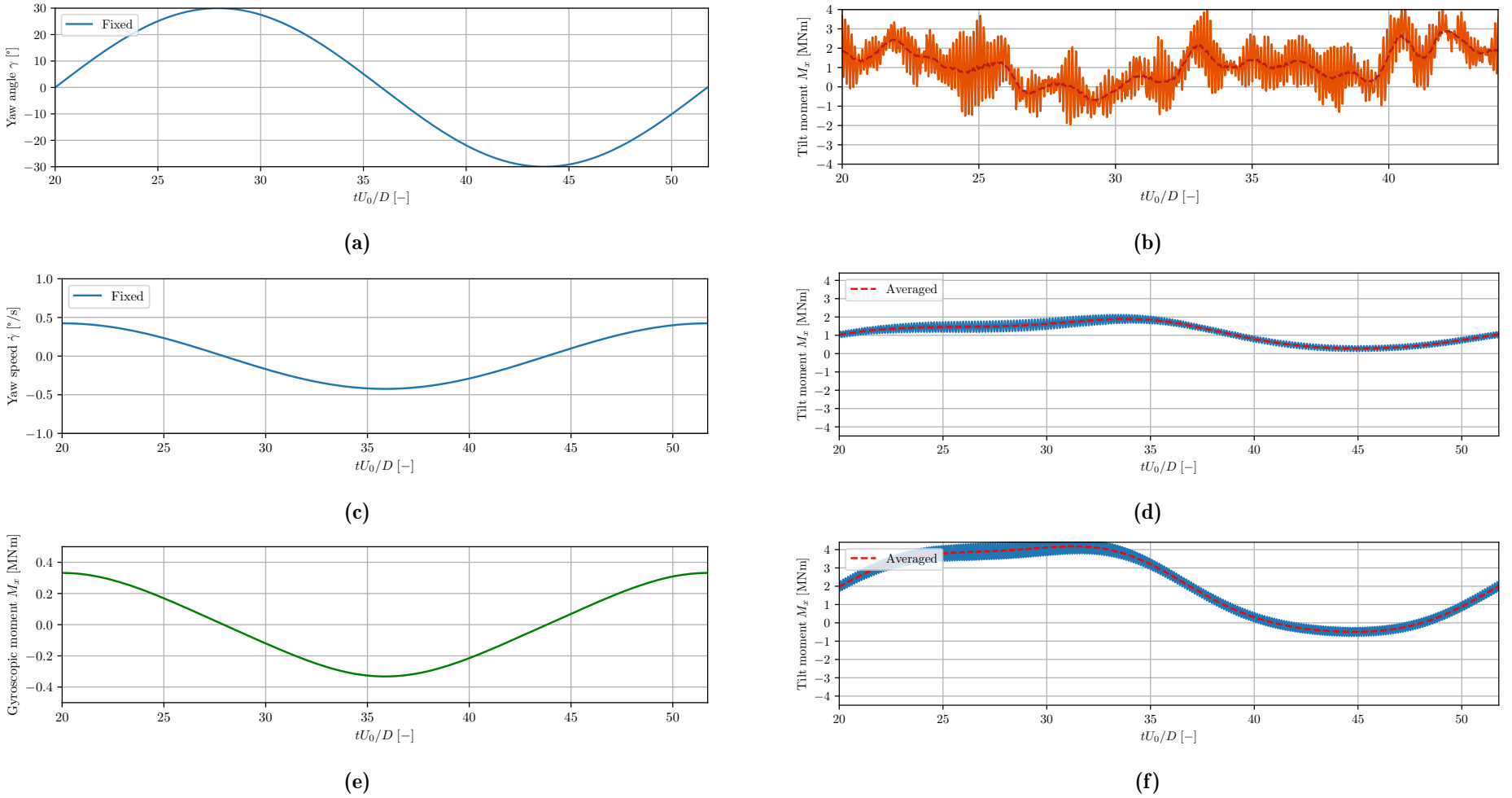

Figure B.5: Imposed yaw angle (a), yaw rate (c) and gyroscopic moment (e) for an inflow of 9 m/s. Tilt moment of the free yaw from previous simulation (b) for comparison. Tilt moment for the imposed yaw kinematic for inflow of 9 m/s (d) and 15 m/s (f). Those two last are from a sheared but without turbulence inflow.

Appendix C

Individual pitch control

Before using the IPC version used in the current manuscript, another version was investigated. The two versions gave different results for some loads. For example, the first one showed decreased DEL for the yaw moment while the second increases it. The version used in the different chapters of this work is the one referenced as the "second version" in this appendix.

This appendix thus aims at explaining the difference between two versions of IPC. The difference is that the first version does not have the filter part (in orange in Figure C.1). The second one features this filtering part and is more in agreement with the literature [24].

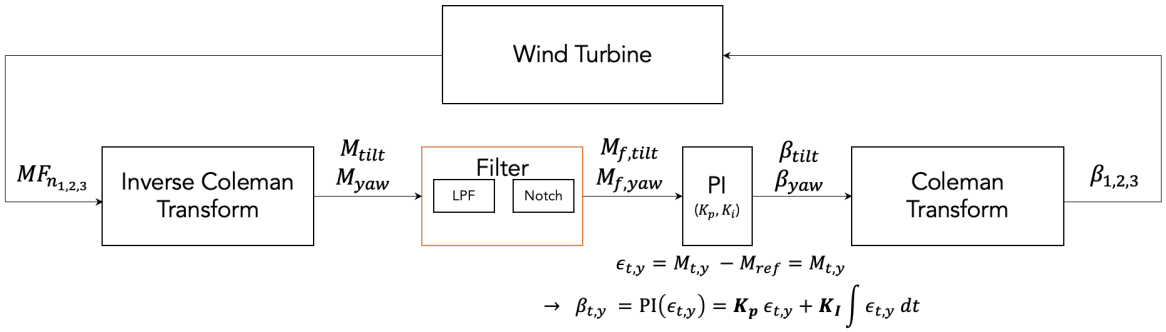

Figure C.1: IPC control loop.

The inputs of IPC are the blades flapwise bending moments ($MF_{n,i}$). The main frequency of those tree blades signals corresponds to the rotation frequency (1P) and are phase-shifted by $\frac{2\pi}{3}$ with respect to each other. They are then translated in a two-axis fixed reference frame with the inverse Coleman transform. It gives two signals (M_{tilt} and M_{yaw}) from the initial tree signals. Those two signals have a large 3P frequency component. The turbulent structures in the inflow then also add low-frequency components to those signals.

The first version of the IPC does not contain any filtering and the PI controller sees all the frequencies of the signals in its inputs. All the frequency content passes through the PI controller and is thus treated. While for the second version the inputs are filtered. The filtering part features a second order low pass filter at 2.5P and a notch filter removing the large 3P component. It is to be noted that the gains of the PI controllers are of importance and that the efficiency of IPC also relies on it. A fine tuning of the gains is required and the efficiency of the chosen gains may also depend on parameters such as the inflow velocity, the turbulence intensity,... Both versions of the IPC have also different gains.

The fatigue loading is quantified with DEL. A loading sample is decomposed in different fatigue cycles of different amplitudes with rainflow counting. Then an equivalent fatigue loading of zero

mean can be evaluated with

$$M_{eq} = \left(\sum_{i=0}^{n_c} \frac{n_i M_{a,i}^m}{N_{eq}} \right)^{1/m} \tag{C.1}$$

where n_i is the number of cycles of amplitude $M_{a,i}$ identified by the rainflow counting, n_c is the number of amplitude bins used for the rainflow counting, N_{eq} is the total amount of cycles considered and m is a parameter depending on the material. The different amplitudes thus have a different weight in the sum, depending on m. Further details can be found in [26, 27].
In Figure C.2, yaw and tilt moments are plotted for the two versions of the IPC. For the tilt moment, both versions of IPC exhibit similar results in term of low frequencies (smaller than 1P) attenuation. The main cause of the tilt moment is shear that is stable in time and the feedback is efficient for both version of IPC. However, the higher frequency content is best reduced with the first version. Indeed, the second version is blind for higher frequencies and cannot have an effect on it. For the yaw moment, it can be further observed that the lower frequency content is less efficiently managed by the first version of IPC. It may be because it is saturated with the high-frequency information caused by turbulence. The feedback is thus too slow and less prone to deal with the lower frequencies. This difference in low-frequency reduction can be observed with the FFTs of the different signal, in Figure C.3. Moreover, in all the cases, version 2 seems to slightly amplify frequencies around 3P.

Those differences in the efficiency regarding lower or higher frequencies have an impact on the quantification of the fatigue loading. Both versions mitigate the loads differently. With the exponent m all the amplitudes/frequencies are considered with a different weight compared to the others. That is why in some cases, the use of IPC leads to DEL that are more important than without using it. For example for the first version, IPC leads to a reduction by 27.9% of the yaw moment DEL. In the case of the second versions it leads to an increase of 13.7 %. However as depicted in Figure C.2, the second version is much more efficient at reducing low-frequency content.

The aim of IPC is to reduce 1P loads on turbine blades. Even if this second version best fulfils what is expected from it, it is not especially translated in terms of DEL reduction here. More work should also maybe done on the PI controller gains tuning.

	$\mathbf{M_{yaw}}$ **DEL**		$\mathbf{M_{tilt}}$ **DEL**	
IPC	Off	On	Off	On
Version 1	1.1×10^{64}	4.8×10^{62}	3.6×10^{64}	1.5×10^{62}
Version 2	8.5×10^{63}	5.0×10^{63}	3.9×10^{64}	2.5×10^{64}

Table C.1: Result for $\sum_{i=0}^{n_c} n_i M_{a,i}^m$ $[Nm]$, with $m = 10$ for the different IPC versions.

	$\mathbf{M_{yaw}}$ **DEL**		$\mathbf{M_{tilt}}$ **DEL**	
IPC	Off	On	Off	On
Version 1	1.8×10^{26}	4.7×10^{25}	3.6×10^{64}	5.3×10^{25}
Version 2	1.8×10^{26}	3.0×10^{26}	2.8×10^{26}	3.4×10^{26}

Table C.2: Result for $\sum_{i=0}^{n_c} n_i M_{a,i}^m$ $[Nm]$, with $m = 4$ for the different IPC versions.

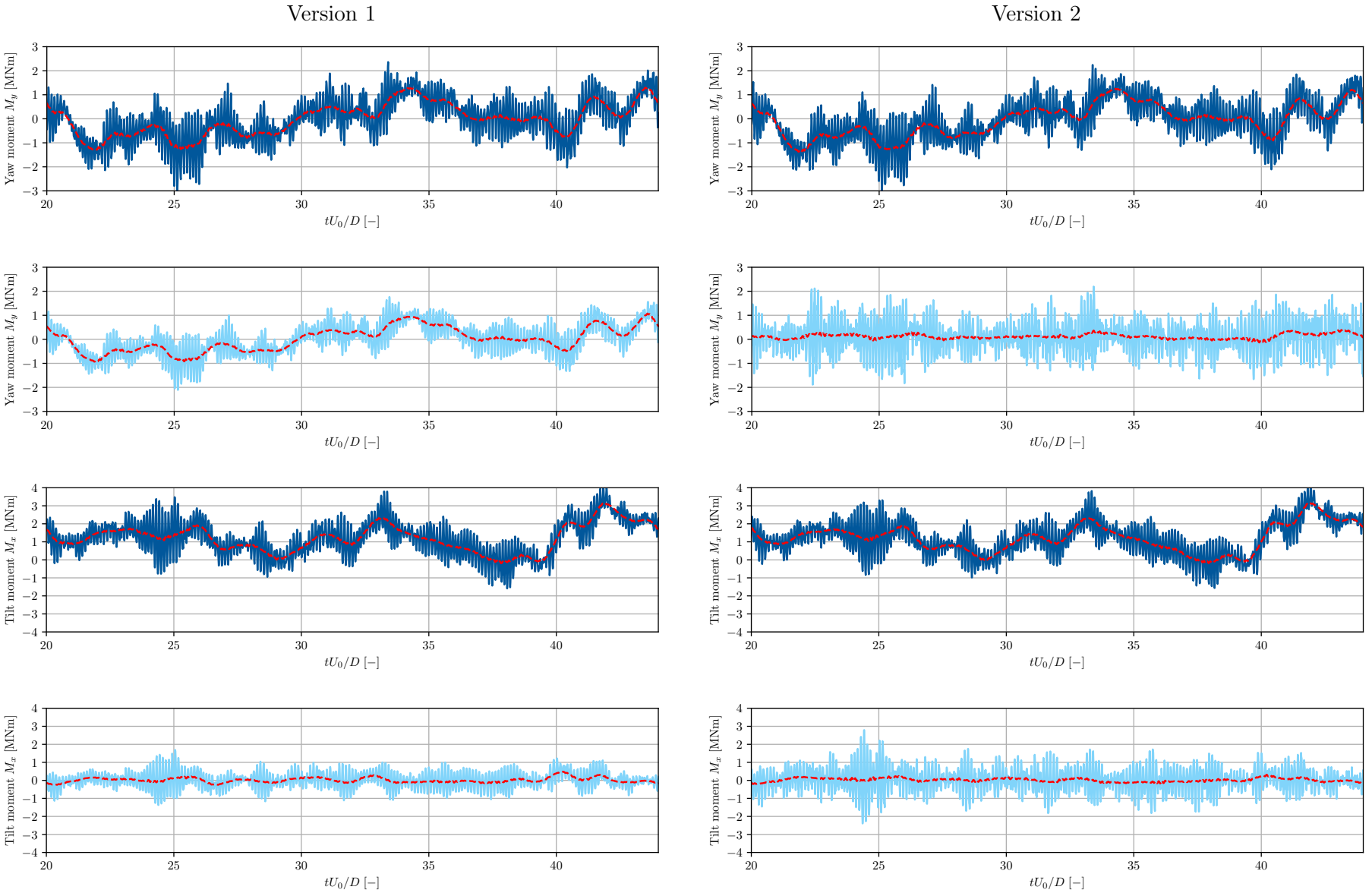

Figure C.2: Yaw and tilt moments obtained for the first and the second version of the IPC, respectively in the first and second column. Light blue corresponds to the cases with IPC.

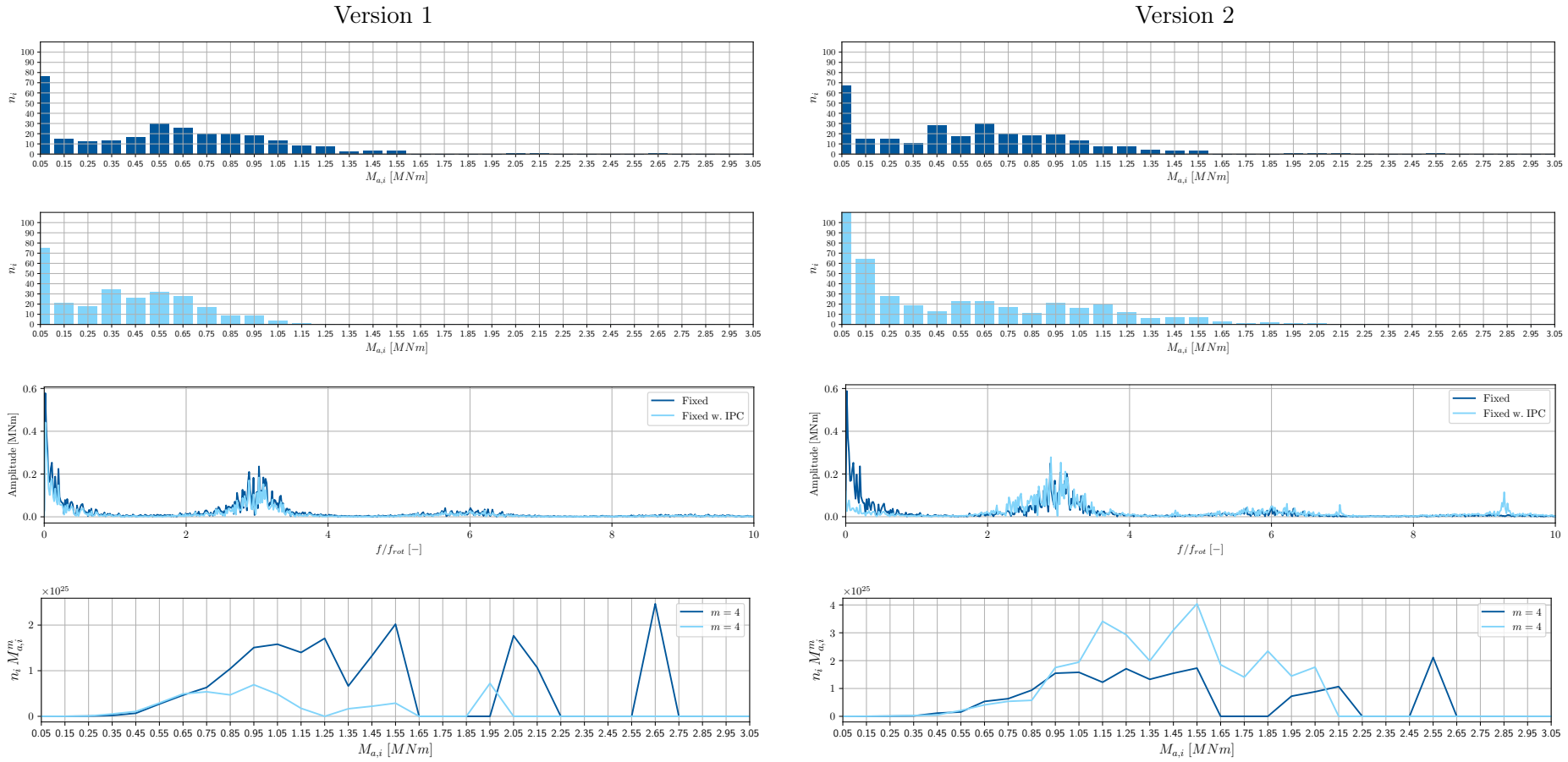

Figure C.3: Yaw moments analysis for the two IPC versions. The bar chart represents the result of the rainflow counting. The third graph is the fft of the yaw moment and the last one is $n_i\, M_{a,i}^m$ that goes in the sum of Equation C.1. Light blue corresponds to the cases with IPC.

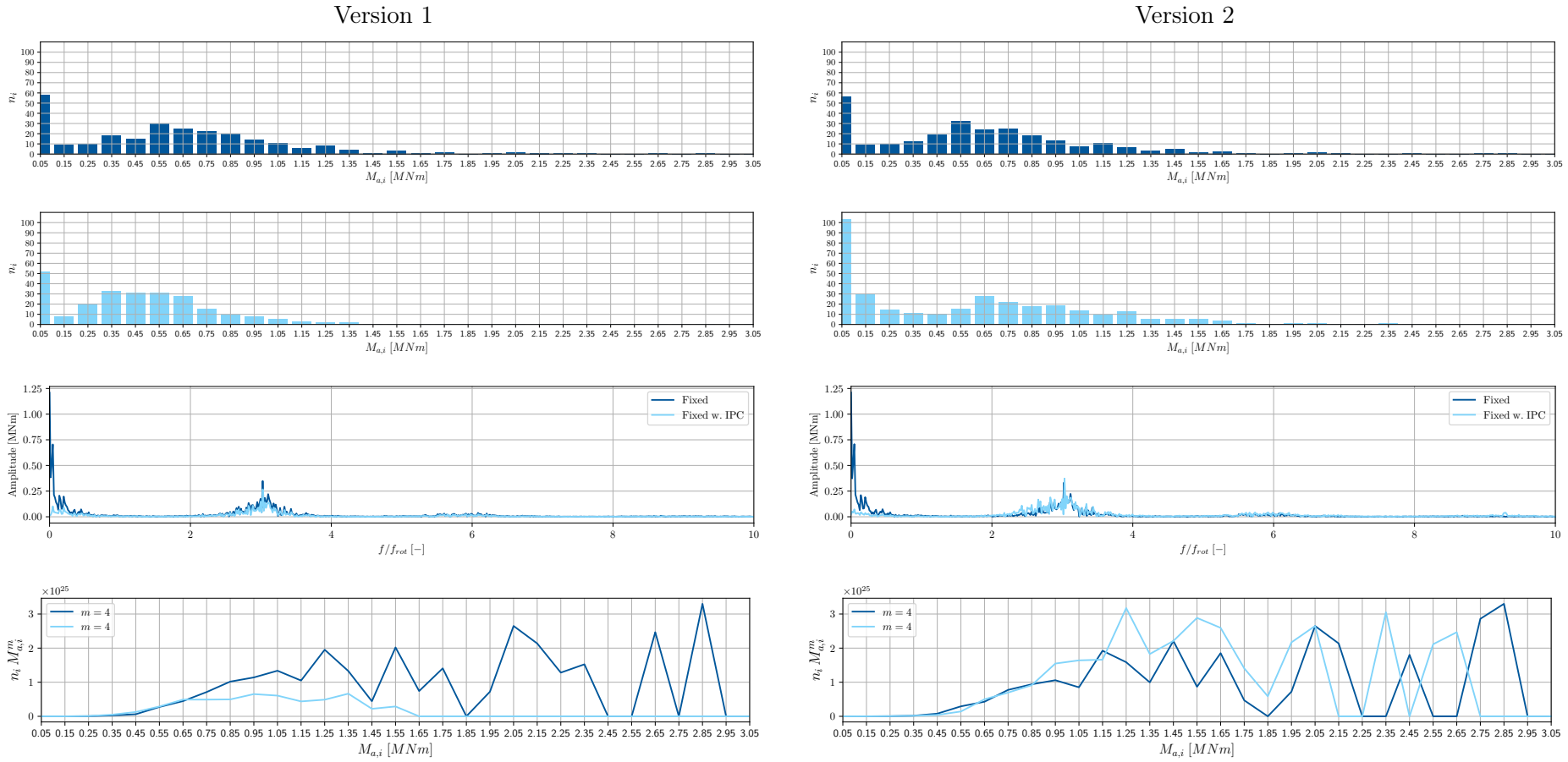

Figure C.4: Tilt moment analysis for the two IPC versions. The bar chart represents the result of the rainflow counting. The third graph is the fft of the tilt moment and the last one is $n_i\, M_{a,i}^m$ that goes in the sum of Equation C.1. Light blue corresponds to the cases with IPC.

UNIVERSITÉ CATHOLIQUE DE LOUVAIN
École polytechnique de Louvain
Rue Archimède, 1 bte L6.11.01, 1348 Louvain-la-Neuve, Belgique | **www.uclouvain.be/epl**